Localized hexagon patterns of the planar Swift–Hohenberg equation

David J.B. Lloyd
Department of Mathematics
University of Surrey
Guildford, GU2 7XH, UK

Björn Sandstede
Department of Mathematics
University of Surrey
Guildford, GU2 7XH, UK

Daniele Avitabile
Department of Engineering Mathematics
University of Bristol
Bristol BS8 1TR, UK

Alan R. Champneys
Department of Engineering Mathematics
University of Bristol
Bristol BS8 1TR, UK

June 5, 2008

Abstract

We investigate stationary spatially localized hexagon patterns of the two-dimensional Swift–Hohenberg equation in the parameter region where the trivial state and regular hexagon patterns are both stable. Using numerical continuation techniques, we trace out the existence regions of fully localized hexagon patches and of planar pulses which consist of a strip filled with hexagons that is embedded in the trivial state. We find that these patterns exhibit snaking: for each parameter value in the snaking region, an infinite number of patterns exist that are connected in parameter space and whose width increases without bound. Our computations also indicate a relation between the limits of the snaking regions of planar hexagon pulses with different orientations and of the fully localized hexagon patches. To investigate which hexagons among the one-parameter family of hexagons are selected in a hexagon pulse or front, we derive a conserved quantity of the spatial dynamical system that describes planar patterns which are periodic in the transverse direction and use it to calculate the Maxwell curves along which the selected hexagons have the same energy as the trivial state. We find that the Maxwell curve lies within the snaking region as expected from heuristic arguments.

Keywords: Localized patterns, hexagons, spots, Turing bifurcation, Swift-Hohenberg equation

AMS subject classification: 35B32, 35B35, 35J60

1 Introduction

Localized stationary structures play an important role in many biological, chemical and physical processes (see, for instance, the textbooks [45, 72, 74]). Such structures have been observed in a variety of experiments ranging from vertically vibrated granular materials [38, 89], liquid crystals [15], binary-fluid convection [8, 65], autocatalytic chemical reactions such as the Belousov–Zhabotinsky system [31, 90], electrochemical systems [1, 6], and localized micro-structures in solidification [48] to nonlinear optical devices [63, 77, 86]. Localized patterns have also been found in many nonlinear models such as those derived from magnetohydrodynamics [12], flame fronts [39], lasers [56], vibrated granular materials [36, 88], neural networks [54, 55], and cellular buckling [47] as well as in the Swift–Hohenberg equation [26, 28, 29, 44, 80], which often serves as a paradigm for general pattern-forming systems [30, 37].

In this paper, we consider stationary solutions of the Swift–Hohenberg equation [30, 85]

$$u_t = -(1+\Delta)^2 u - \mu u + \nu u^2 - u^3 \tag{1.1}$$

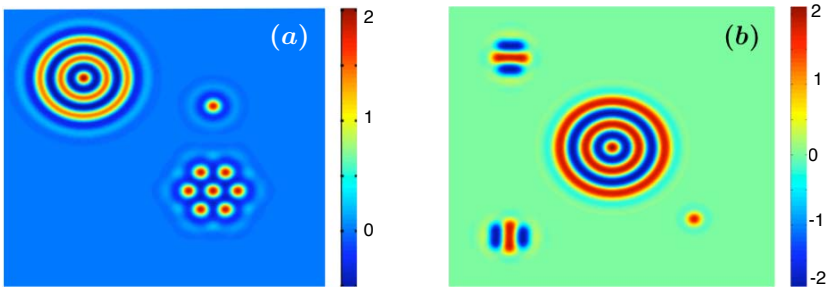

Figure 1: *(a) Localized stationary spots and hexagon patches of (1.1) for* $(\mu, \nu) = (0.5, 2.2)$. *(b) Localized stationary spots and stripes of (1.5) for* $(\mu, \nu) = (2.5, 4)$. *Both images are color plots of stationary solutions* $u(x, y)$, *with* x *plotted horizontally and* y *vertically, where the values of* $u(x, y)$ *are represented by colors as indicated in the color bars shown to the right of the color plots: the color plots in the remainder of this paper are produced in the same fashion.*

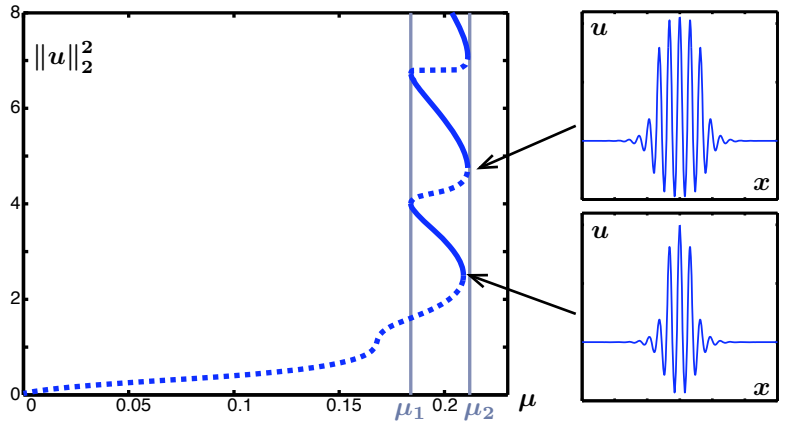

Figure 2: *A partial bifurcation diagram of localized stationary patterns in the 1D Swift–Hohenberg equation (1.1) is shown for* $\nu = 1.6$ *(other solution branches are given in Figure 8 below). Dotted blue lines indicate (temporally) unstable solutions, while solid blue lines denote stable solutions. At each fold along the snake, a pair of new rolls is formed in the pulse. The left and right fold bifurcations approach the vertical asymptotes* $\mu_1 = 0.181$ *and* $\mu_2 = 0.211$, *and the Maxwell point is* $\mu_M = 0.2$.

where $x \in \mathbb{R}$ for the 1D version and $(x, y) \in \mathbb{R}^2$ in the planar case. We focus on the region $\nu \geq 0$ since the case $\nu < 0$ is then recovered upon replacing u by $-u$. The trivial state $u = 0$ is stable for $\mu > 0$ and destabilizes at $\mu = 0$ with respect to perturbations that have nonzero finite spatial wavelength. At $\mu = 0$, hexagons bifurcate in a transcritical bifurcation from $u = 0$ for each $\nu > 0$, while rolls bifurcate in a subcritical pitchfork bifurcation from $u = 0$ provided $\nu > \nu_r := \sqrt{27/38}$ [44]. While the bifurcating hexagons and rolls are initially unstable for $\mu > 0$, they stabilize in a subsequent saddle-node bifurcation, leading to bistability between the nontrivial patterns and the trivial state for $\mu > 0$. The bistability of trivial and patterned states opens up the possibility of finding fully localized stationary patches of hexagons or rolls such as those shown in Figure 1. It is patterns of this type that we shall focus on in this paper.

We first review briefly the situation in 1D and refer to §2 for a more extensive discussion. In one space dimension, the Swift–Hohenberg equation exhibits localized structures as shown in Figure 2. The patterns shown there are connected in parameter space, and their width increases as we move up on the bifurcation curve: this scenario is referred to as *snaking* [92]. There are several interesting questions one may ask about the patterns shown in Figure 2: can we predict for which values of μ these structures exist, and can we determine *a priori* which periodic pattern is selected to form the localized structure?

We begin with the second question: the steady-state equation

$$-(1 + \partial_x^2)^2 u - \mu u + \nu u^2 - u^3 = 0 \tag{1.2}$$

of the 1D Swift–Hohenberg equation exhibits, in the relevant parameter region, a one-parameter family of periodic patterns for each fixed (μ, ν). To decide which one of these makes up the core of the localized structure, we consider a front that connects the trivial state to a periodic pattern: this front corresponds to a heteroclinic orbit of the ordinary differential equation (1.2) that connects $u = 0$ to a periodic orbit. It turns out that the ODE (1.2) admits the first integral

$$\mathcal{H}(u) = u_{xxx}u_x - \frac{u_{xx}^2}{2} + u_x^2 + \frac{(1+\mu)u^2}{2} - \frac{\nu u^3}{3} + \frac{u^4}{4} \tag{1.3}$$

so that the value $[\mathcal{H}(u)](x)$ of $\mathcal{H}$ along a solution $u(x)$ of (1.2) does not change as a function of x. In particular, if we evaluate $\mathcal{H}$ along our front, we find that $\mathcal{H}$ must vanish along the limiting periodic pattern as it vanishes at $u = 0$. Generically, $\mathcal{H}$ will vanish only at finitely many periodic orbits in the family of periodic patterns and will therefore serve as a selection principle that involves only the periodic patterns.

We now address the first question, namely for which parameter values stationary fronts exist. We recall that the Swift–Hohenberg equation (1.1) posed on $\mathbb{R}^d$ with $1 \le d \le 3$ is a gradient system,

$$u_t = -\nabla\mathcal{E}(u),$$

in $H^2(\mathbb{R}^d)$, where the energy functional $\mathcal{E}$ is given by

$$\mathcal{E}(u) = \int_{\mathbb{R}^d} \left[\frac{[(1+\Delta)u]^2}{2} + \frac{\mu u^2}{2} - \frac{\nu u^3}{3} + \frac{u^4}{4} \right] \mathrm{d}\mathbf{x}, \qquad \mathbf{x} \in \mathbb{R}^d \tag{1.4}$$

and the gradient $\nabla\mathcal{E}(u) = \frac{\delta\mathcal{E}}{\delta u}(u)$ of $\mathcal{E}$ with respect to u is computed in $L^2(\mathbb{R}^d)$. In particular, $\mathcal{E}$ decreases strictly in time along solutions of (1.1) unless the solution is stationary. We record that the existence of the first integral $\mathcal{H}$ given above is actually a consequence of the translation invariance of the integrand of $\mathcal{E}$. While we cannot evaluate the energy functional along periodic patterns as they are not localized whence the integral in (1.4) may not exist, we may, however, define a local energy by integrating over one spatial period of the underlying periodic pattern. We may then expect, on a heuristic level, that stationary interfaces between the trivial state and the periodic pattern can exist only when their local energies coincide: otherwise, one of the states would invade the other one to decrease energy, thus leading to moving fronts. This gives a heuristic criterion that allows us to determine for which values of μ stationary fronts can exist: for each μ, compute the periodic pattern $u_*(\mu)$ for which $\mathcal{H}(u_*(\mu)) = 0$, calculate its local energy $\mathcal{E}(u_*(\mu))$, and then find μ so that $\mathcal{E}(u_*(\mu)) = 0$. The corresponding parameter value μ_{M} is referred to as the Maxwell point. It was first pointed out by Pomeau [73] that stationary fronts should exist not only at the Maxwell point $\mu = \mu_{\mathrm{M}}$ but in an entire interval that contains μ_{M} where fronts are pinned or locked. Consequently, we expect to find localized roll patches in an entire interval, and this is what happens in Figure 2. The specific pinning mechanism leading to Figure 2 was elucidated in [26, 52, 92] and will be discussed in §2.

We now turn to the planar Swift–Hohenberg equation (1.1). Several numerical observations of localized spots and hexagon patches of (1.1) have been documented in the literature [26, 44, 78]. Localized square patterns have also been observed in the Swift–Hohenberg equation when an additional nonlinear gradient term is added [44, 79]. In addition, localized stripes and spots have been found in the cubic-quintic Swift–Hohenberg equation

$$u_t = -(1+\Delta)^2 u - \mu u + \nu u^3 - u^5. \tag{1.5}$$

Close to our approach is the paper [63] in which a complex Ginzburg–Landau equation with a saturable nonlinearity was studied in a cavity-soliton context. In [63], the steady-state equation was solved numerically as a boundary-value problem, and the bifurcation diagram was traced out for various localized patterns, including hexagon patches, using continuation techniques. However, the authors continued solutions only up to the first fold and not beyond.

The aim of this paper is to investigate hexagon fronts and fully localized hexagon patches in the 2D Swift–Hohenberg equation (1.1). We have three main results. The first is the construction of a conserved quantity $\mathcal{H}$ for the 2D Swift–Hohenberg equation: the existence of $\mathcal{H}$ is a consequence of Noether's theorem since the integrand of the energy functional $\mathcal{E}$ is invariant under translations, i.e. does not depend explicitly on x.

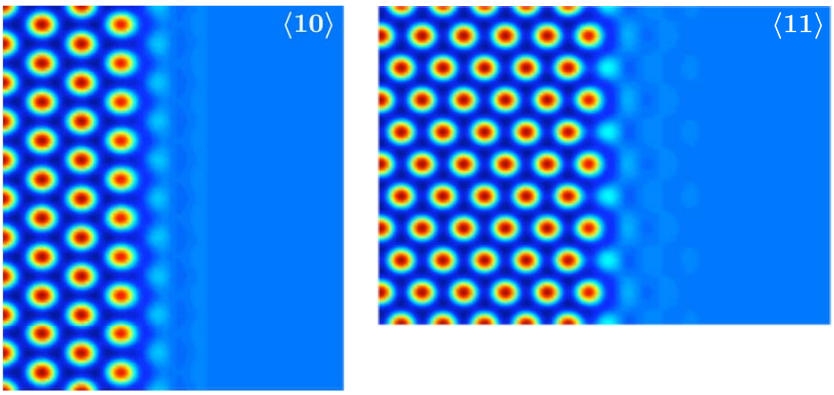

Figure 3: *Color plots of two stationary fronts are shown for the planar Swift–Hohenberg equation (1.1): both fronts connect hexagons to the trivial state along the horizontal x-direction, are periodic in the vertical y-direction, and differ in the way in which their interfaces are aligned in a fixed hexagonal lattice.*

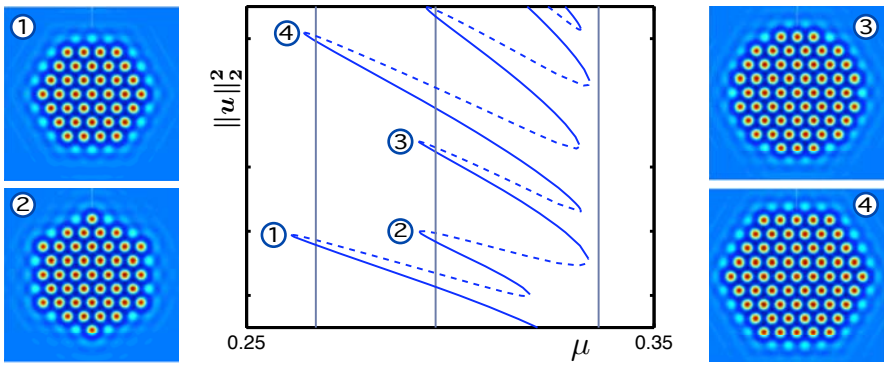

Figure 4: *Part of the bifurcation curve corresponding to localized hexagon patches of (1.1) with $\nu = 1.6$ is shown. Color plots of representative solutions are shown in panels 1-4. The entire snaking curve and color plots of the associated stationary solutions can be viewed in this [MOVIE].*

Proposition 1 (Conserved quantity for the 2D Swift–Hohenberg equation) *If $u(x, y)$ is a smooth solution of the planar Swift–Hohenberg equation (1.1) which is spatially periodic with period ℓ in the y-variable, then the quantity*

$$\mathcal{H}(u) = \int_0^\ell \left[u_{xxx}u_x - \frac{u_{xx}^2}{2} + u_x^2 + \frac{(1+\mu)u^2}{2} - \frac{\nu u^3}{3} + \frac{u^4}{4} - u_{xy}^2 - u_y^2 + \frac{u_{yy}^2}{2} \right] \mathrm{d}y \tag{1.6}$$

does not depend on x.

As in the 1D case, the first integral $\mathcal{H}$ provides a selection principle for hexagons: if we find a planar front that connects hexagons to the trivial state and is periodic in the transverse direction, see Figure 3, then $\mathcal{H}$ must vanish when evaluated along a single hexagon in the far field of the front. This selection principle together with the local energy $\mathcal{E}$ will allow us to compute Maxwell points for the planar Swift–Hohenberg equation (1.1). Our second result shows that, for each fixed $\nu > 0$, and all sufficiently small $\mu > 0$, there is a unique small-amplitude hexagon pattern along which $\mathcal{H}$ vanishes. We refer to §3.3 for a stronger result.

Proposition 2 (Existence of hexagons with $\mathcal{H} = 0$) *For each fixed $\nu > 0$, there is a number $\mu_0 > 0$ so that the planar Swift–Hohenberg equation (1.1) admits a unique small-amplitude hexagon solution $u_*(\mu)$ that satisfies $\mathcal{H}(u_*(\mu)) = 0$ for each $\mu \in (0, \mu_0)$. These hexagons satisfy $u_*(0) = 0$, have wavenumber $\kappa_*(\mu)$ with $\kappa_*(0) = 1$, and depend smoothly on μ.*

Our third result is a comprehensive numerical study of localized hexagon patches in the planar Swift–Hohenberg equation (1.1). Instead of giving a detailed list of these results, which can be found in §5, we

focus here on the observation that these localized structures snake:

Observation 1 (Snaking of localized hexagon patches) *Localized hexagon patches of the Swift–Hohenberg equation exist and snake in a wedge-shaped region in the (μ,ν)-parameter plane. The shape of the hexagon patches changes along the snaking curve: their interfaces resemble planar hexagon fronts with different orientations with respect to a fixed hexagonal lattice; see Figures 3 and 4. The saddle-node bifurcations of the localized hexagon patches are aligned with saddle-nodes of planar hexagon fronts which are shown as vertical lines in Figure 4.*

The remainder of this paper is organized as follows. We begin in §2 with a review of snaking in one space dimension as this case motivated our paper to a large extent. We also review known results about regular hexagons and planar hexagon fronts. In §3, we discuss selection principles for hexagons and prove Propositions 1 and 2. We outline in §4 the numerical algorithms that we used to compute planar hexagon fronts and localized hexagon patches and comment on their implementation. Our main results can be found in §5, where we discuss fully localized hexagon and rhomboid patches. We end in §6 with conclusions and a discussion.

Throughout this paper, we use color plots to illustrate the profiles of stationary planar patterns and refer to the caption of Figure 1 for an explanation of what these plots represent. Two-parameter bifurcation diagrams are always drawn using (μ,ν^2) rather than (μ,ν) which makes the diagrams more legible.

2 Review of 1D snaking and planar hexagons

2.1 Snaking in one space dimension

Recall the steady-state equation

$$-(1+\partial_x^2)^2 u - \mu u + \nu u^2 - u^3 = 0, \qquad x \in \mathbb{R} \tag{2.1}$$

of the 1D Swift–Hohenberg equation (1.1). Equation (2.1) has two important features that we shall exploit: it is invariant under the reflection $x \mapsto -x$ and admits the first integral $\mathcal{H}$ given in (1.3).

At $\mu = 0$, the trivial state $u = 0$ undergoes a pitchfork bifurcation to even spatially periodic patterns with period 2π or wavenumber $\kappa = 1$. These patterns bifurcate supercritically with $\mu < 0$ when $\nu < \nu_r := \sqrt{27/38}$ and subcritically with $\mu > 0$ when $\nu > \nu_r$. To accommodate the switch from super- to subcritical at $\nu = \nu_r$, a fold of periodic patterns with wavenumber $\kappa = 1$ emerges from $(\mu,\nu) = (0,\nu_r)$ into the positive half-plane

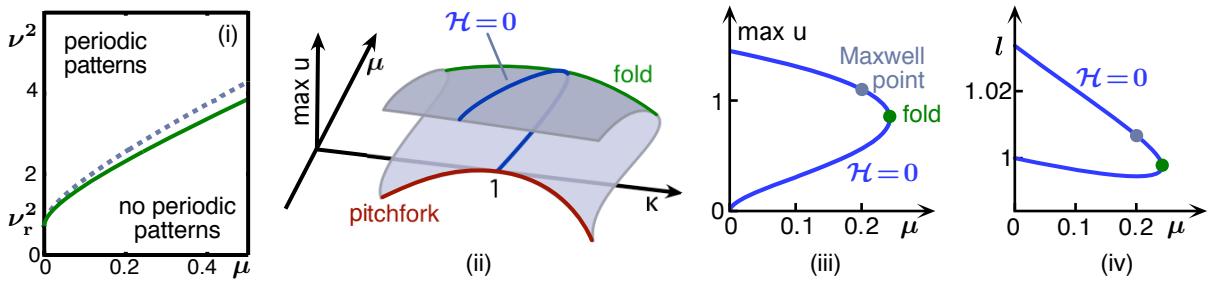

Figure 5: *Panel (i) contains the numerically computed fold bifurcation curve of 1D rolls of (2.1) with wavenumber $\kappa = 1$ [solid green] and the Maxwell curve [dotted grey] along which rolls with $\mathcal{H} = 0$ and $\mathcal{E} = 0$ exist. The schematic picture in panel (ii) indicates that, for fixed $\nu > \nu_r$, rolls exist for any wavenumber κ close to one. Panels (iii) and (iv) contain numerical bifurcation diagrams of the rolls that satisfy $\mathcal{H} = 0$ for $\nu = 1.6$: shown are the amplitude and the wavelength $l = 1/\kappa$ (so that $l = 1$ corresponds to a period of 2π). The Maxwell point $\mathcal{E} = 0$ occurs on the upper branch where rolls are stable.*

as shown in Figure 5(i). In fact, even periodic patterns bifurcate for any wavenumber κ close to one along a curve of pitchfork bifurcations, as indicated in Figure 5(ii) for a fixed $\nu > \nu_{\mathrm{r}}$.

We are interested in standing localized structures such as those shown in Figure 2. As argued in §1, the Maxwell curve predicts parameter regions where these structures may exist [11, 68, 70]: recall that Maxwell points are found by calculating, for each given (μ, ν), the periodic roll pattern $u_{\mathrm{per}}(\mu, \nu)$ that has vanishing first integral $\mathcal{H} = 0$ and subsequently adjusting the parameters so that the energy $\mathcal{E}(u_{\mathrm{per}}(\mu, \nu))$, computed over one period of u_{per}, vanishes as well. This can be done numerically, and the result [17, 19] is the Maxwell curve shown in Figure 5(i) which emerges from the codimension-two point $(0, \nu_{\mathrm{r}})$ where the bifurcation to rolls changes from super- to subcritical. We give two arguments that show that the Maxwell curve can emerge only from this point. First, small-amplitude rolls are unstable at subcritical bifurcations, while they bifurcate for $\mu < 0$ at supercritical bifurcations: in neither case can we find stable rolls for $\mu > 0$ that co-exist with the stable trivial state. Alternatively, the normal form at pitchfork bifurcations is $\mu w - a w^3 = 0$, and the associated energy $\mathcal{E}(w) = \mu w^2/2 - a w^4/4$ does not vanish at the bifurcating state when $a \neq 0$.

Around the Maxwell curve, a pinning region exists where stable localized patterns can be found [73]. We shall now briefly review two different approaches that explain why this pinning region is present and why snaking occurs.

Asymptotics beyond all orders. Near the codimension-two point $(\mu, \nu) = (0, \nu_{\mathrm{r}})$ with $\nu_{\mathrm{r}} = \sqrt{27/38}$, the snaking behavior in (1.1) can be explained by the interaction between the underlying periodic state and the slowly varying envelope which forms the localized structure. On the level of amplitude equations, the fast scale of the underlying periodic pattern is ignored, and these amplitude equations then predict that stationary pulses exist only at the Maxwell point. In the works [11, 13], the fast scale was formally re-introduced at lowest order into the amplitude equation and the effect on locking and pinning analysed. This approach predicts an exponentially small width of the order $\exp(-\pi/|\nu - \nu_{\mathrm{r}}|^2)$ of the locking region in the parameter μ when $\nu > \nu_{\mathrm{r}}$ is fixed with $|\nu - \nu_{\mathrm{r}}| \ll 1$, but does not capture the precise asymptotic behavior in ν. A consistent asymptotic analysis beyond all orders was recently carried out in [25, 52] which gives the precise asymptotic behavior of the width of the locking region in the parameter μ as a function of ν as ν approaches ν_{r}. Multiple scale expansions that capture the different scaling regimes near the bifurcation point and the Maxwell curve in one step, albeit without addressing terms beyond all orders, were introduced earlier in [16, 17]; in addition, the wavelength correction along the Maxwell curve was calculated in [17, (3.27)].

Dynamical-systems geometry. The second approach we shall discuss is of a more geometric nature and due to [26, 92]. We rewrite the fourth-order steady-state equation (2.1) as the first-order system

$$U_x = F(U; \mu, \nu), \qquad U = (u, u_x, u_{xx}, u_{xxx}) \in \mathbb{R}^4 \tag{2.2}$$

where we regard x as the time-like evolution variable. Recall that (2.2) has the first integral $\mathcal{H}$ from (1.3). The reflection invariance $x \mapsto -x$ of (2.1) means that (2.2) is reversible with reverser $\mathcal{R}U := (u, -u_x, u_{xx}, -u_{xxx})$: if $U(x)$ is a solution, so is $\mathcal{R}U(-x)$. Reversible solutions $U(x)$ of (2.2), which by definition satisfy $U(0) \in \operatorname{Fix}\mathcal{R}$, correspond to even solutions $u(x)$ of (2.1).

The trivial state $u = 0$ and the even periodic patterns $u_{\mathrm{per}}(x)$ of (2.1) correspond to the equilibrium $U = 0$ and reversible periodic orbits $U_{\mathrm{per}}(x)$, respectively, of (2.2). If the trivial state $u = 0$ and the rolls $u_{\mathrm{per}}(x)$ are temporally stable with respect to the Swift–Hohenberg equation, then the corresponding solutions $U = 0$ and $U_{\mathrm{per}}(x)$ of (2.2) are hyperbolic. If, for instance, $U = 0$ was not hyperbolic, then the matrix $F_U(0; \mu, \nu)$ would have a purely imaginary eigenvalue $\mathrm{i}\omega$, and $u(x, t) = \mathrm{e}^{\mathrm{i}\omega x}$ would satisfy the linearization of (1.1) about $u = 0$, which contradicts temporal stability. A similar argument applies to purely imaginary Floquet exponents of $U_{\mathrm{per}}(x)$, which are related to the dispersion relation of $u_{\mathrm{per}}(x)$: if the rolls $u_{\mathrm{per}}(x)$ are spectrally stable, then the periodic orbit $U_{\mathrm{per}}(x)$ will have only two Floquet exponents at zero; see [66, 67, 82, 83] and [81, §3.4.2] for further details. In summary, we can identify the localized patterns $u_{\mathrm{loc}}(x)$ shown in Figure 2

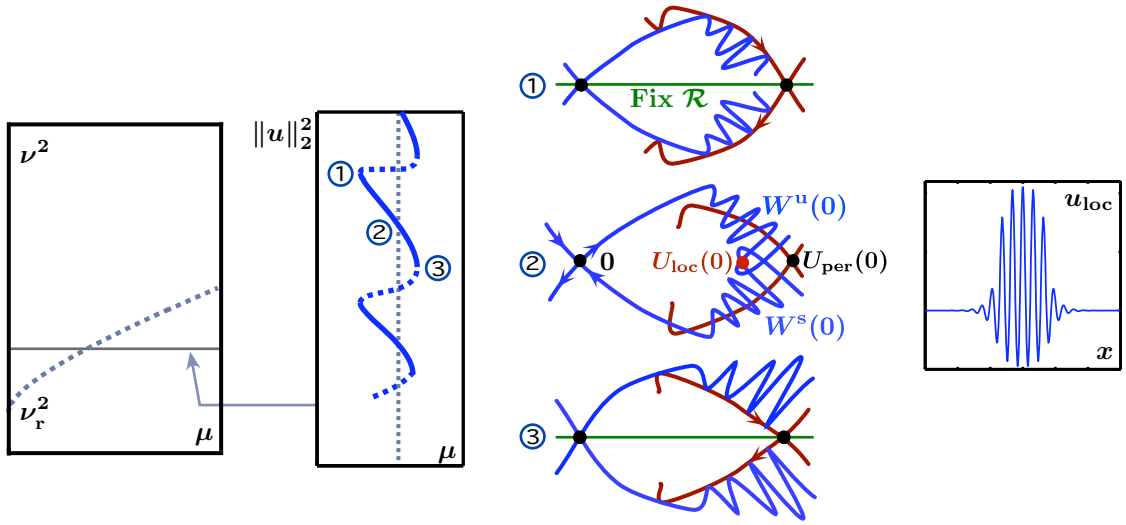

Figure 6: *The left-most panel shows the Maxwell curve in the (μ, ν^2)-parameter space, while the center-left panel shows the bifurcation diagram for a fixed value of ν. The three pictures in the center-right panel illustrate the geometry of the stable and unstable manifolds of the equilibrium $U = 0$ and the periodic orbit U_{per} in a two-dimensional Poincare section [see text for further details]: the tangles in the unstable and stable manifolds of $U = 0$ are caused by the expansion and contraction near the periodic orbit and are therefore more pronounced near the periodic orbit. The localized pattern shown in the right-most panel corresponds to the intersection U_{loc} of the stable and unstable manifolds of $U = 0$ near the periodic orbit U_{per}.*

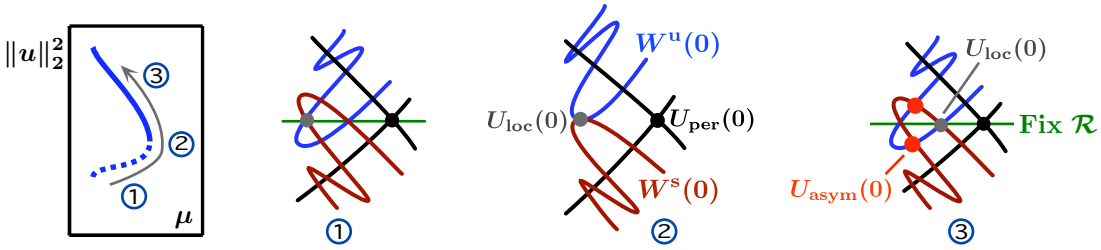

Figure 7: *As we move upwards on the snaking curve, μ first increases and then decreases. Geometrically, the localized structure moves from one branch of the invariant manifolds through a saddle-node bifurcation to the adjacent branch. In doing so, it moves closer to the periodic orbit: thus, it spends more 'time' x near U_{per} and therefore broadens in space. As a result, its norm increases which explains the structure of the snaking curve. Besides saddle-node bifurcations, the localized structures also undergo pitchfork bifurcations which result in two asymmetric structures explained further in the text and in Figure 8.*

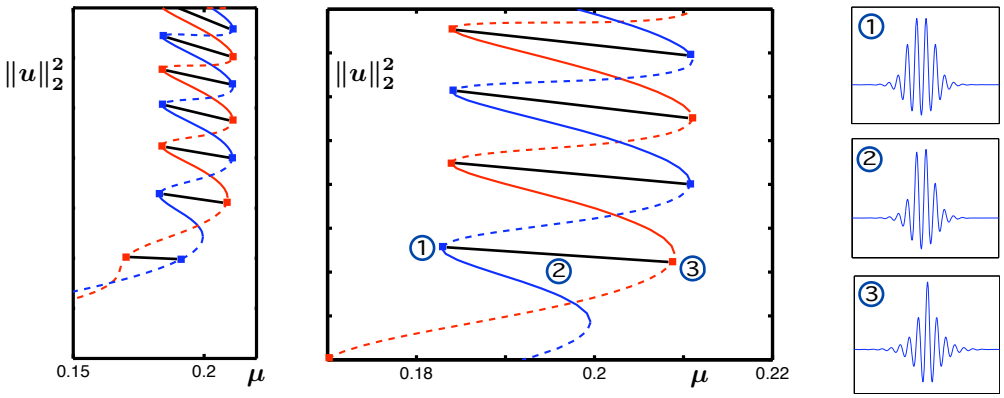

Figure 8: *The left and center panels contain the bifurcation diagrams of asymmetric localized structures that bifurcate at pitchfork bifurcations from even localized structures [20, 22]: solutions along the curved branches are even with minima [blue] or maxima [red] at $x = 0$, while solutions along the horizontal ladders [black] are asymmetric. Panels 1-3 contain the graphs of selected solution profiles $u(x)$.*

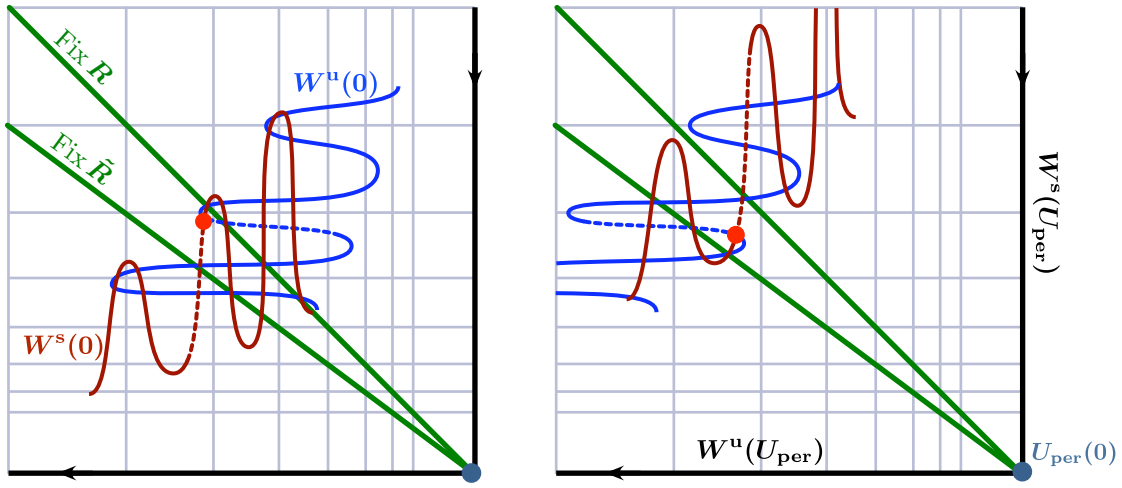

Figure 9: *Shown is the dynamics of the linearized Poincaré map near the periodic orbit* U_{per}*. On the left, the parameter* μ *is close to the pitchfork bifurcation in* $\mathrm{Fix}\,\mathcal{R}$ *that creates an asymmetric localized structure* $U_{\mathrm{asym}}(0)$ *[red bullet]. As* μ *is increased, we assume that* $W^{\mathrm{u}}(0)$ *is moved to the left and, correspondingly, by reversibility,* $W^{\mathrm{s}}(0)$ *is moved upwards. Following their intersection* $U_{\mathrm{asym}}(0)$*, which occurs along the branches plotted with dashes, we observe that it ends at a second pitchfork bifurcation in* $\mathrm{Fix}\,\tilde{\mathcal{R}}$*. Thus, the asymmetric localized structures connect, in parameter space, even solutions with a minimum at* $x = 0$ *to even solutions with a maximum at* $x = 0$*. The points* $U_{\mathrm{asym}}(0)$ *stay on the same horizontal and vertical segments of the invariant manifolds, and their distance from* $U_{\mathrm{per}}(0)$ *does therefore not change much: in particular, their* L^2*-norm cannot change by too much, which explains why the ladders are approximately horizontal. [*MOVIE*].*

with homoclinic orbits of (2.2) that lie in the intersections of the stable and unstable manifolds of $U = 0$ which come close to the hyperbolic periodic orbit $U_{\mathrm{per}}(x)$.

To visualize this situation better, we restrict (2.2) to the three-dimensional invariant zero level set $\mathcal{H}^{-1}(0)$ of the first integral $\mathcal{H}$. Next, we choose a two-dimensional Poincaré section Σ in the three-dimensional set $\mathcal{H}^{-1}(0)$ at the point $U_{\mathrm{per}}(0)$ on the periodic orbit $U_{\mathrm{per}}(x)$. The fixed-point space $\mathrm{Fix}\,\mathcal{R}$ of the reverser $\mathcal{R}$ becomes a line in the section Σ which can be used to identify symmetric orbits: note that the phase diagrams will be symmetric under the reverser $\mathcal{R}$. We now make the assumption that the unstable manifold of $U = 0$ intersects the stable manifold of the periodic orbit $U_{\mathrm{per}}(x)$ transversely in the section Σ and that the parameter μ moves these manifolds transversely through each other[1] as shown in Figure 6. Numerical computations in [42] confirmed this assumption in the snaking regime of a reversible system of two coupled second-order equations. Figure 6 illustrates the resulting geometry which explains why the existence region of localized structures is an interval in parameter space. The end points of the intervals correspond to parameter values where fronts that connect the trivial state to the patterned state disappear in saddle-node bifurcations. Figure 7 explains in more detail why the localized structures get broader as we move up along the snaking curve.

As can be seen from Figure 7, the reflection symmetry $x \mapsto -x$ of the Swift–Hohenberg equation has another interesting consequence: each saddle-node bifurcation of an even localized structure is accompanied by a pitchfork bifurcation at which two asymmetric structures bifurcate. In the Swift–Hohenberg equation, these asymmetric states and the associated bifurcation diagrams were recently computed numerically in [20, 22], and we reproduce their numerical computations in Figure 8. As shown in Figure 8, the asymmetric structures connect two different families of even localized structures in parameter space. We give now a brief heuristic explanation of this phenomenon and refer to [10] for a rigorous approach. Here and in [10], we assume that the parameter μ unfolds the intersection of $W^{\mathrm{u}}(0)$ and $W^{\mathrm{s}}(U_{\mathrm{per}})$ as indicated in Figure 6 and that the resulting bifurcation diagram of even localized structures is as shown in Figure 8. Each symmetric

[1] Due to reversibility, the same is then true for the stable manifold of $U = 0$ and the unstable manifold of $U_{\mathrm{per}}(x)$

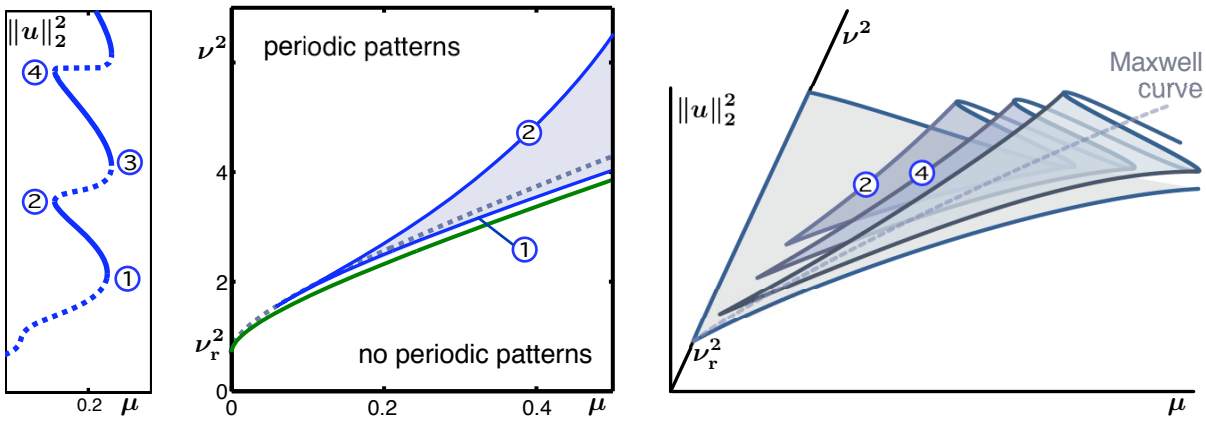

Figure 10: *The middle panel contains the numerically computed fold curves of localized rolls of (2.1) associated with the folds labelled (1) and (2) in the left panel: the two fold curves collide in a cusp bifurcation. The right panel contains a schematic illustration of the sheet of localized rolls: fold curves of localized rolls will collide pairwise in cusps, and we believe that the sequence of cusps approaches the codimension-two point* $(0, \nu_r)$ *along the Maxwell curve.*

periodic orbit $U_{\mathrm{per}}(x)$ intersects the fixed-point space $\mathrm{Fix}\,\mathcal{R}$ precisely twice, and the two intersection points correspond to maxima and minima of u_{per}. Even localized structures arise as intersections of the unstable manifold $W^{\mathrm{u}}(0)$ with $\mathrm{Fix}\,\mathcal{R}$ either near the maximum or the minimum of U_{per}. In the Swift–Hohenberg equation, numerical evidence suggests that both these structures exist; see Figure 8. To capture them, we can work with two different Poincaré sections Σ_{max} and Σ_{min}, placed at the maximum and minimum, or else work with a second reverser $\tilde{\mathcal{R}} := \Pi\mathcal{R}\Pi^{-1}$ near the section $\Sigma := \Sigma_{\mathrm{min}}$ where $\Pi : \Sigma_{\mathrm{max}} \to \Sigma_{\mathrm{min}}$ is the first-return map induced by the flow of (2.2). We choose the latter approach as it allows us to visualize the entire dynamics in one section. We straighten out the invariant manifolds of U_{per} and use the linearized Poincaré map near the symmetric orbit U_{per}. Using the assumptions made above on the unfolding of the intersections with respect to the parameter μ, we obtain the diagrams shown in Figure 9 which reproduce the numerically observed ladder structure geometrically.

We now turn to a discussion of the shape of the snaking region in the (μ, ν)-parameter space. Figure 6 indicates that snaking occurs in an interval in μ that is bounded by fold bifurcations of heteroclinic orbits which connect $U = 0$ to the rolls $U_{\mathrm{per}}(x)$. To demarcate the snaking region in (μ, ν)-space, we should therefore continue these fold bifurcations in parameter space, which is a difficult numerical task as we would need to find simultaneously periodic solutions, their Floquet eigenfunctions, and the heteroclinic orbits at a structurally unstable saddle-node bifurcation (see [53] for a recent numerical approach to this problem). Instead, we continue fold bifurcations of localized rolls in the parameters (μ, ν). As shown in Figure 10, these fold curves do not reach the codimension-two point $(\mu, \nu) = (0, \nu_r)$ but instead collide pairwise in cusp bifurcations. Continuing fold curves of localized rolls therefore gives a good approximation of the snaking region which fails, however, near the codimension-two point.

2.2 Regular hexagonal patterns

We briefly review known results on the existence and stability of regular hexagons ([33, 40, 41, 49]; see also [35, §2] for a review), which can be tiled to cover the entire plane.

The planar Swift–Hohenberg equation

$$u_t = -(1 + \Delta)^2 u - \mu u + \nu u^2 - u^3, \qquad \mathbf{x} = (x, y) \in \mathbb{R}^2 \tag{2.3}$$

is equivariant under the action of the Euclidean symmetry group $\mathbb{E}(2)$ which consists of rotations, translations, and reflections of the plane. Thus, we may seek stationary solutions to this equation that are invariant

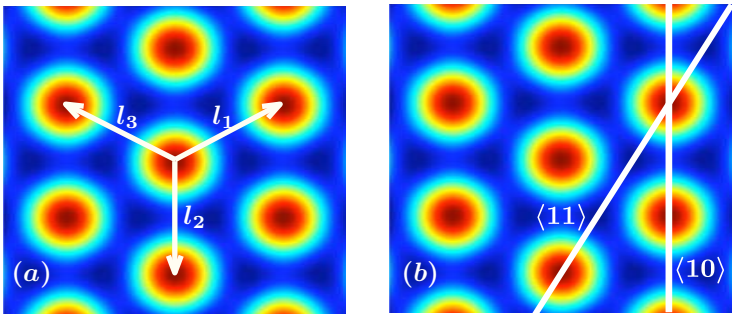

Figure 11: *Shown are color plots of regular hexagons on the lattice $\mathcal{L}$ together with the lattice vectors l_1, l_2, and l_3 in panel (a) and with two lines with Bravais–Miller indices $\langle 10\rangle$ and $\langle 11\rangle$ in panel (b).*

under a given fixed subgroup of $\mathbb{E}(2)$. We focus on hexagons with wavenumber $\kappa = 1$ and consider therefore the planar hexagonal lattice $\mathcal{L}$

$$\mathcal{L} = \{n_1 l_1 + n_2 l_2 + n_3 l_3 \in \mathbb{R}^2;\ n_1, n_2, n_3 \in \mathbb{Z}\},$$

where

$$l_1 = 2\pi\left(1, \frac{1}{\sqrt{3}}\right), \qquad l_2 = 2\pi\left(0, -\frac{2}{\sqrt{3}}\right), \qquad l_3 = 2\pi\left(-1, \frac{1}{\sqrt{3}}\right);$$

see Figure 11. It is convenient to retain the lattice vector l_3 even though it is redundant. Hexagons are time-independent solutions $u(\mathbf{x})$ of (2.3) which are invariant under the subgroup $\mathbb{D}_6$ of $\mathbb{E}(2)$ and which are $\mathcal{L}$-periodic so that

$$u(\mathbf{x} + l) = u(\mathbf{x}) \qquad \forall l \in \mathcal{L},\ \forall \mathbf{x} \in \mathbb{R}^2.$$

To find hexagons, it is convenient to use the dual lattice $\mathcal{L}^*$ defined via

$$\mathcal{L}^* = \{n_1 k_1 + n_2 k_2 + n_3 k_3 \in \mathbb{R}^2;\ n_1, n_2, n_3 \in \mathbb{Z}\}$$

with

$$k_1 = (-1, 0), \qquad k_2 = \left(\frac{1}{2}, \frac{\sqrt{3}}{2}\right), \qquad k_3 = \left(\frac{1}{2}, -\frac{\sqrt{3}}{2}\right)$$

which allows us to represent $\mathcal{L}$-periodic solutions of (2.3) by the Fourier series

$$u(\mathbf{x}, t) = \sum_{k \in \mathcal{L}^*} \hat{u}_k(t) \mathrm{e}^{\mathrm{i}k\cdot\mathbf{x}}.$$

We now restrict our attention to hexagons that bifurcate from $u = 0$. Linearizing (2.3) about $u = 0$ gives the linear operator $-(1+\Delta)^2 - \mu$. Posed on appropriate spaces of $\mathcal{L}$-periodic functions, the first instability occurs at $\mu = 0$ where an eigenvalue of algebraic multiplicity six, with eigenfunctions $\exp(\pm \mathrm{i} k_j \cdot \mathbf{x})$ for $j = 1, 2, 3$, crosses into the right half-plane. On the resulting six-dimensional center manifold, we can parametrize solutions as

$$u(\mathbf{x}, t) = A_1(t)\mathrm{e}^{-\mathrm{i}x} + A_2(t)\mathrm{e}^{\mathrm{i}(x+\sqrt{3}y)/2} + A_3(t)\mathrm{e}^{\mathrm{i}(x-\sqrt{3}y)/2} + h(A_1, A_2, A_3, \overline{A}_1, \overline{A}_2, \overline{A}_3; \mu, \nu) + \text{c.c.}, \tag{2.4}$$

where the function h represents the higher-order contributions to the center manifold. The flow on the center manifold can be calculated for $|\mu| \ll 1$ and $|\nu| \ll 1$ by evaluating the Swift–Hohenberg equation on the elements of the center manifold and projecting the resulting expression back onto the center eigenspace[2]. The result is

$$\begin{aligned}
\dot{A}_1 &= -\mu A_1 + \alpha_1 \overline{A}_2 \overline{A}_3 + \alpha_2 A_1 |A_1|^2 + \alpha_3 A_1 (|A_2|^2 + |A_3|^2) + r(A_1, A_2, A_3) \\
\dot{A}_2 &= -\mu A_2 + \alpha_1 \overline{A}_1 \overline{A}_3 + \alpha_2 A_2 |A_2|^2 + \alpha_3 A_2 (|A_1|^2 + |A_3|^2) + r(A_2, A_3, A_1) \\
\dot{A}_3 &= -\mu A_3 + \alpha_1 \overline{A}_2 \overline{A}_1 + \alpha_2 A_3 |A_3|^2 + \alpha_3 A_3 (|A_2|^2 + |A_1|^2) + r(A_3, A_1, A_2)
\end{aligned} \tag{2.5}$$

[2]If ν is small, then the function h is not needed for the calculation of the cubic terms of the reduced vector field: the coefficients in (2.5) for arbitrary ν can be found in [44]

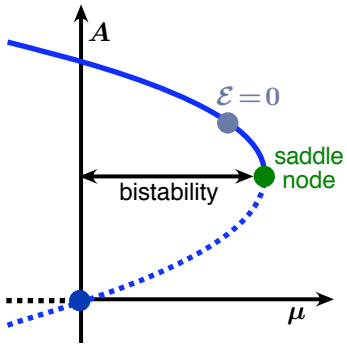

Figure 12: *The bifurcation diagram of hexagons with critical wavenumber $\kappa = 1$ in the Swift–Hohenberg equation is shown for fixed $0 < \nu \ll 1$. Solid lines correspond to stable patterns, while dotted lines correspond to unstable ones. The hexagons undergo a saddle-node bifurcation at amplitude $A = \nu/15 + \mathrm{O}(\nu^2)$ when $\mu = \nu^2/15 + \mathrm{O}(\nu^3)$. The energy $\mathcal{E}$ vanishes only for $\mu = \mu_{\mathcal{E}}$ given in (2.9) for the hexagons with amplitude $A = 4\nu/45 + \mathrm{O}(\nu^2)$ on the upper branch.*

plus the complex conjugated equations of six ODEs for the complex amplitudes A_j, where the coefficients α_j are real and given by

$$\alpha_1 = 2\nu + \mathrm{O}(|\mu|(|\mu| + |\nu|)), \qquad \alpha_2 = -3 + \mathrm{O}(|\mu| + |\nu|), \qquad \alpha_3 = -6 + \mathrm{O}(|\mu| + |\nu|),$$

and the remainder term $r(z) = \mathrm{O}(|z|^4)$ is of higher order. Equivariance of the Swift–Hohenberg equation and invariance of the hexagonal lattice with respect to rotations by $\pi/3$, reflections, and translations manifest themselves in the equivariance of the reduced system with respect to the transformations

$$\begin{aligned}
\sigma &: (A_1, A_2, A_3) \mapsto (\overline{A}_3, \overline{A}_1, \overline{A}_2) \\
\rho &: (A_1, A_2, A_3) \mapsto (A_1, A_3, A_2) \\
\tau_a &: (A_1, A_2, A_3) \mapsto (\mathrm{e}^{\mathrm{i}a_1} A_1, \mathrm{e}^{-\mathrm{i}(a_1+\sqrt{3}a_2)/2} A_2, \mathrm{e}^{\mathrm{i}(-a_1+\sqrt{3}a_2)/2} A_3),
\end{aligned}$$

respectively. Hexagons are invariant under $\mathbb{D}_6$ and therefore lie, in particular, in the one-dimensional intersection of the fixed-point spaces of σ^2 and σ^3, which is given by $A := A_1 = A_2 = A_3 \in \mathbb{R}$. As an intersection of fixed-point spaces, the line $A_1 = A_2 = A_3 \in \mathbb{R}$ is invariant under (2.5), and hexagons can therefore be found as nontrivial equilibria of the differential equation

$$\dot{A} = -\mu A + 2\nu A^2 - 15A^3 + \mathrm{O}((|\mu| + |\nu|)(|\mu| + |A|)|A|^2 + |A|^4) \tag{2.6}$$

which exist for

$$\mu = 2\nu A - (15 + \mathrm{O}(|\nu| + |A|))A^2. \tag{2.7}$$

The stability of these hexagons with respect to $\mathcal{L}$-periodic perturbations is calculated by considering the linearization of (2.5) about the hexagons [23, 40]. The resulting bifurcation diagram of hexagons is plotted for $\nu > 0$ in Figure 12; other solution branches corresponding to mixed modes, which bifurcate in secondary bifurcations, and rolls exist but are not shown in Figure 12. The hexagons with $A > 0$ shown in Figure 12 are up-hexagons: our focus is on $\mu, \nu > 0$ and we shall therefore encounter only up-hexagons in the rest of this paper. When $\nu < 0$, the bifurcation diagram in Figure 12 does not change except that A is reflected via $A \mapsto -A$: in this case, localized hexagon patterns consist of down-hexagons though the bifurcation diagrams shown in the remainder of the paper would not change due to the symmetry $(u, \nu) \mapsto (-u, -\nu)$.

We now calculate the energy $\mathcal{E}(u)$ given in (1.4) along the hexagon branch (2.7). Substituting

$$u(x, y) = 2A\left[\cos(x) + \cos((x + \sqrt{3}y)/2) + \cos((x - \sqrt{3}y)/2)\right]$$

into (1.4) and integrating over the fundamental domain $[0, 4\pi] \times [0, 4\pi/\sqrt{3}]$, we find that the energy of the hexagons with wavenumber $\kappa = 1$ is given by

$$\mathcal{E} = \frac{8\pi^2 A^3}{\sqrt{3}}(4\nu - 45A) + \mathrm{O}((|\nu| + |A|)A^4) \tag{2.8}$$

which vanishes precisely when $A = 4\nu/45 + \mathrm{O}(\nu^2)$, which corresponds to the parameter curve

$$\mu_{\mathcal{E}} = \frac{8\nu^2}{135} + \mathrm{O}(\nu^3). \tag{2.9}$$

For fixed $\nu > 0$, the energy (2.8) along the bifurcating hexagons is strictly larger than zero for $0 < |A| \ll 1$.

Throughout this section, we considered only hexagons with wavenumber $\kappa = 1$. Hexagons with wavenumbers κ close to one bifurcate for $\mu = -(1-\kappa^2)^2$, and these can be captured by an analogous analysis upon using the arguments $(\kappa x, \kappa y)$ in place of (x, y) in the right-hand side of (2.4).

2.3 Planar hexagon fronts

We now discuss planar stationary hexagon fronts that connect hexagons to the trivial state. As illustrated in Figure 3, these fronts can have different orientations with respect to the hexagonal lattice $\mathcal{L}$, which can be classified using the Bravais–Miller index [5]:

Definition 1 (Bravais–Miller index) *Fix the hexagonal lattice $\mathcal{L}$. The Bravais–Miller index $\langle n_1\, n_2\, n_3\rangle$ of a line in the plane is given by the reciprocals n_j of the intercepts of the line with the lines $\mathbb{R}l_j$ generated by the lattice vectors l_j (assigning the reciprocal $n_j = 0$ if the line does not intersect $\mathbb{R}l_j$). Negative indices $-n$ with $n > 0$ are conventionally written as $\overline{n} := -n$. Since $n_1 + n_2 + n_3 = 0$, we may write the index using only two indices: our choice is $\langle n_1\, n_2\rangle$, and we refer to Figure 11(b) for examples.*

If a hexagon front has a straight interface, we assign the Bravais–Miller index of its interface to it. Two examples of Bravais–Miller indices are given in Figure 11(b), and the corresponding hexagon fronts are shown in Figure 3. We shall present more detailed numerical results for the existence of fronts with these orientations later in the paper.

For μ close to zero, stationary fronts between hexagons and the trivial state can be found using a formal multi-scale expansion as carried out in [60], though we note that this approach cannot capture the expected pinning and locking of these fronts. To construct stationary $\langle 10\rangle$ fronts, we substitute the ansatz

$$u(x,y) = \epsilon\left(A_1(\epsilon x)\mathrm{e}^{-\mathrm{i}x} + A_2(\epsilon x)\left[\mathrm{e}^{\mathrm{i}(x+\sqrt{3}y)/2} + \mathrm{e}^{\mathrm{i}(x-\sqrt{3}y)/2}\right] + \text{c.c.}\right)$$

into (2.3), set $\mu = \epsilon^2\tilde{\mu}$ and $\nu = \epsilon\tilde{\nu}$, and expand in powers of ϵ. To leading order, we obtain the system

$$\begin{aligned} 0 &= 4\partial_X^2 A_1 - \tilde{\mu}A_1 + 2\tilde{\nu}\overline{A}_2^2 - 3A_1|A_1|^2 - 12A_1|A_2|^2 \\ 0 &= \partial_X^2 A_2 - \tilde{\mu}A_2 + 2\tilde{\nu}\overline{A}_1\overline{A}_2 - 9A_2|A_2|^2 - 6A_2|A_1|^2 \end{aligned} \tag{2.10}$$

where the nonlinearity on the right-hand side comes from (2.5) upon setting $A_2 = A_3$. A similar ODE can be derived for $\langle 11\rangle$ fronts and, in fact, for fronts of any given orientation [60].

Stationary fronts with index $\langle 10\rangle$ that connect the trivial state to hexagons with wavenumber $\kappa = 1$ correspond to heteroclinic orbits of (2.10) that connect $(A_1, A_2) = (0,0)$ to the hexagon solutions $(A_1, A_2) = (\tilde{A}, \tilde{A})$ where $A = \epsilon\tilde{A}$ is an equilibrium of (2.6). Equation (2.10) admits the first integral

$$\begin{aligned} \mathcal{H}(A_1, A_2) &= 2|\partial_X A_1|^2 + |\partial_X A_2|^2 - \tilde{\mu}\left(\frac{|A_1|^2}{2} + |A_2|^2\right) \\ &\quad + \tilde{\nu}(\overline{A}_1\overline{A}_2^2 + A_1A_2^2) - \frac{3}{4}|A_1|^4 - 6|A_1|^2|A_2|^2 - \frac{9}{2}|A_2|^4 \end{aligned} \tag{2.11}$$

which is constant along solutions of (2.10). In particular, heteroclinic orbits between $(0,0)$ and $(\tilde{A}, \tilde{A})$ can exist only when $\mathcal{H}(\tilde{A}, \tilde{A}) = \mathcal{H}(0,0) = 0$ which gives the condition

$$\mathcal{H}(\tilde{A}, \tilde{A}) = -\frac{3\tilde{\mu}}{2}\tilde{A}^2 + 2\tilde{\nu}\tilde{A}^3 - \frac{45}{4}\tilde{A}^4 = 0$$

that we need to solve for $\tilde{A}$. Using (2.7) and interpreting the results in the original unscaled parameters, we arrive at the condition

$$\mu_{\mathrm{M}} = \frac{8\nu^2}{135} + \mathrm{O}(\nu^3) \tag{2.12}$$

along which $\mathcal{H}$ vanishes at the bifurcating hexagons with wavenumber $\kappa = 1$. Equation (2.9) shows that the energy $\mathcal{E}$ vanishes at the same hexagons for the same parameter values, to the order in which we computed them. Thus, the curve defined by (2.12) gives the Maxwell curve, which provides a heuristic criterion for the existence of planar fronts but does not account for pinning and locking phenomena.

The analysis reviewed here is valid only in the limit $(\mu, \nu) \to 0$ and does not address the wavenumber selection as we fixed $\kappa = 1$. In §3, we will construct a conserved quantity $\mathcal{H}$ which defines the Maxwell curve for general parameter values and prove Proposition 3 on the selection of hexagons that satisfy $\mathcal{H} = 0$. In §5.2, we shall compare the predictions made by the Maxwell curve (2.12) and its extension from §3 with numerical computations for the full 2D Swift–Hohenberg equation.

3 Spatial dynamics, and selection principles for hexagons

In this section, we prove Propositions 1 and 2.

3.1 Proof of Proposition 1

Proposition 1 states that if $u(x, y)$ is a bounded solution of the planar stationary Swift–Hohenberg equation

$$-(1+\Delta)^2 u - \mu u + \nu u^2 - u^3 = 0, \qquad (x, y) \in \mathbb{R}^2 \tag{3.1}$$

which is spatially periodic with period ℓ in the y-variable, then the quantity

$$\mathcal{H}(u) = \int_0^\ell \left[u_{xxx} u_x - \frac{u_{xx}^2}{2} + u_x^2 + \frac{(1+\mu)u^2}{2} - \frac{\nu u^3}{3} + \frac{u^4}{4} - u_{xy}^2 - u_y^2 + \frac{u_{yy}^2}{2} \right] \mathrm{d}y \tag{3.2}$$

does not depend on x. This can, of course, be verified directly by computing the derivative of (3.2) with respect to x and using (3.1), and we omit this straightforward calculation.

Instead, we outline how the first integral $\mathcal{H}$ can be derived in the first place from the translation invariance of the Lagrangian associated with (3.1) and refer to [2, 3] and [24, Ch. 15] for a general abstract approach. We start with a general energy functional[3]

$$\mathcal{E}(u) = \int_{\mathbb{R}^d} \mathcal{L}(u(\mathbf{x}), \nabla u(\mathbf{x}), \Delta u(\mathbf{x}))\, \mathrm{d}\mathbf{x}, \qquad \mathbf{x} = (x_1, \ldots, x_d) \in \mathbb{R}^d$$

where $\mathcal{L}(q, p, r) : \mathbb{R} \times \mathbb{R}^d \times \mathbb{R} \to \mathbb{R}$ is a given smooth function that does not depend explicitly upon $\mathbf{x}$. The Euler–Lagrange equation associated with the energy functional $\mathcal{E}$ reflects the extremum condition $\nabla \mathcal{E}(u) = \frac{\delta \mathcal{E}}{\delta u}(u) = 0$, where the gradient with respect to u is calculated in the L^2-scalar product, and is given by

$$\mathcal{L}_q(u, \nabla u, \Delta u) - \nabla \cdot \mathcal{L}_p(u, \nabla u, \Delta u) + \Delta \mathcal{L}_r(u, \nabla u, \Delta u) = 0, \qquad \mathbf{x} = (x_1, \ldots, x_d) \in \mathbb{R}^d, \tag{3.3}$$

where the partial derivatives $\mathcal{L}_q$, $\mathcal{L}_p$ and $\mathcal{L}_r$ of the function $\mathcal{L}(q, p, r)$ are evaluated at $(u(\mathbf{x}), \nabla u(\mathbf{x}), \Delta u(\mathbf{x}))$. Assume now that $u(\mathbf{x})$ is a smooth solution of the Euler–Lagrange equation (3.3). We compute

$$\begin{aligned}
\frac{\mathrm{d}}{\mathrm{d}x_1} \left[\mathcal{L}(u, \nabla u, \Delta u) \right] &= \mathcal{L}_q u_{x_1} + \mathcal{L}_p \cdot \nabla u_{x_1} + \mathcal{L}_r \Delta u_{x_1} \\
&\overset{(3.3)}{=} (\nabla \cdot \mathcal{L}_p - \Delta \mathcal{L}_r) u_{x_1} + \mathcal{L}_p \cdot \nabla u_{x_1} + \mathcal{L}_r \Delta u_{x_1} \\
&= u_{x_1} \nabla \cdot \mathcal{L}_p + \nabla u_{x_1} \cdot \mathcal{L}_p + \mathcal{L}_r \Delta u_{x_1} - (\Delta \mathcal{L}_r) u_{x_1} \\
&= \nabla \cdot (u_{x_1} \mathcal{L}_p) + \nabla \cdot (\mathcal{L}_r \nabla u_{x_1} - u_{x_1} \nabla \mathcal{L}_r).
\end{aligned}$$

Thus, we have established the existence of a conservation law for the Euler–Lagrange equation.

[3] In §3.1, we use $\mathcal{L}$ exclusively for the Lagrangian; in all other sections, this letter refers to the hexagonal lattice

Lemma 1 *Assume that $u(\mathbf{x})$ is a smooth solution of the Euler–Lagrange equation (3.3) associated with the Lagrangian $\mathcal{L}(q,p,r)$, then the conservation law*

$$\partial_{x_1}\mathcal{L}(u,\nabla u,\Delta u)-\nabla\cdot[u_{x_1}\mathcal{L}_p(u,\nabla u,\Delta u)+\mathcal{L}_r(u,\nabla u,\Delta u)\nabla u_{x_1}-u_{x_1}\nabla\mathcal{L}_r(u,\nabla u,\Delta u)]=0 \tag{3.4}$$

is satisfied for all $\mathbf{x}\in\mathbb{R}^d$.

We now return to the planar Swift–Hohenberg equation (3.1) which is the Euler–Lagrange equation associated with the energy functional

$$\mathcal{E}(u)=\int_{\mathbb{R}^2}\mathcal{L}(u,\nabla u,\Delta u)\,\mathrm{d}x\,\mathrm{d}y$$

for the Lagrangian

$$\mathcal{L}(q,p,r):=\frac{(q+r)^2}{2}+\frac{\mu q^2}{2}-\frac{\nu q^3}{3}+\frac{q^4}{4} \tag{3.5}$$

where $(q,p,r)\in\mathbb{R}\times\mathbb{R}^2\times\mathbb{R}$. Lemma 1 asserts that (3.4) is met for any smooth solution $u(x,y)$ of (3.1). If we further assume that $u(x,y)$ is periodic with period ℓ in y, then we can integrate (3.4) in y over $[0,\ell]$ and use periodicity in y to find that the equation

$$\partial_x\int_0^\ell[\mathcal{L}(u,\nabla u,\Delta u)-u_x\mathcal{L}_{p_1}(u,\nabla u,\Delta u)-\mathcal{L}_r(u,\nabla u,\Delta u)u_{xx}+u_x\partial_x\mathcal{L}_r(u,\nabla u,\Delta u)]\,\mathrm{d}y=0$$

is met for all x, where we write $p=(p_1,p_2)$. In particular, along such solutions,

$$\int_0^\ell[\mathcal{L}(u,\nabla u,\Delta u)-u_x\mathcal{L}_{p_1}(u,\nabla u,\Delta u)-\mathcal{L}_r(u,\nabla u,\Delta u)u_{xx}+u_x\partial_x\mathcal{L}_r(u,\nabla u,\Delta u)]\,\mathrm{d}y$$

does not depend on x. Substituting the expression for $\mathcal{L}$ from (3.5), we find that the integral above coincides with the expression (3.2) for $\mathcal{H}$ as claimed.

3.2 Spatial dynamics

As in the 1D situation, the quantity $\mathcal{H}(u)$ given in (3.2) determines which hexagons can be connected by a stationary planar front to the trivial state. We use spatial dynamics to gain further insight into why snaking should occur for stationary planar fronts. We focus on fronts that connect hexagons to the trivial state and that are spatially periodic along the interface.

Thus, assume that $u(x,y)$ is a smooth solution of (3.1) which is periodic in y with positive minimal period ℓ. We define the wavenumber

$$\kappa=\frac{2\pi}{\ell}$$

and introduce the rescaling $\phi=\kappa y$. With this rescaling, $\phi\in[0,2\pi]$ corresponds to $y\in[0,\ell]$, and the planar Swift–Hohenberg equation (3.1) becomes

$$\partial_x^4u+2\kappa^2\partial_x^2\partial_\phi^2u+\kappa^4\partial_\phi^4u+2(\partial_x^2u+\kappa^2\partial_\phi^2u)+(1+\mu)u-\nu u^2+u^3=0. \tag{3.6}$$

Exploiting that we are now interested in solutions with period 2π in ϕ, we write this equation as a first-order system in x and obtain

$$U_x=\mathcal{A}(\mu,\kappa)U+\mathcal{N}(U;\nu),\qquad U\in\mathcal{U} \tag{3.7}$$

where

$$\mathcal{A}(\mu,\kappa)=\begin{pmatrix}0&1&0&0\\0&0&1&0\\0&0&0&1\\-\kappa^4\partial_\phi^4-2\kappa^2\partial_\phi^2-(1+\mu)&0&-2-2\kappa^2\partial_\phi^2&0\end{pmatrix},\qquad \mathcal{N}(U;\nu)=\begin{pmatrix}0\\0\\0\\\nu U_1^2-U_1^3\end{pmatrix}$$

and $U(x) = U(x)(\varphi)$ is, for each fixed x, a function of φ that lies in $\mathcal{U} := H^3(S^1) \times H^2(S^1) \times H^1(S^1) \times L^2(S^1)$, where S^1 is the interval $[0, 2\pi]$ with the end points identified. Equation (3.7) is reversible with respect to the reverser

$$\mathcal{R}U = \mathcal{R}(U_1, U_2, U_3, U_4)^t = (U_1, -U_2, U_3, -U_4)^t,$$

which corresponds to reflections in x, and admits the first integral

$$\begin{aligned} \mathcal{H}(U; \mu, \nu, \kappa) \quad = \quad & \int_0^{2\pi} \Big[U_2 U_4 - \frac{U_3^2}{2} + U_2^2 + \frac{(1+\mu)U_1^2}{2} - \frac{\nu U_1^3}{3} + \frac{U_1^4}{4} \\ & -\kappa^2 (\partial_\phi U_2)^2 - \kappa^2 (\partial_\phi U_1)^2 + \frac{\kappa^4 (\partial_\phi^2 U_1)^2}{2} \Big] \, \mathrm{d}\phi \end{aligned} \tag{3.8}$$

which is simply (3.2) with y rescaled and $(u, u_x, u_{xx}, u_{xxx})$ replaced by U. Even though the system (3.7) is ill-posed, in the sense that (3.7) may not have a solution for a given initial condition, we can still apply the theory developed in [71, 82, 83] to show that stable and unstable manifolds of equilibria and periodic orbits of (3.7) exist. These manifolds are infinite-dimensional, but the results in [10, 71, 83] imply that the geometric situation for (3.7) is analogous to the 1D situation.

The existence of the first integral $\mathcal{H}$ implies that if there is a heteroclinic orbit of (3.7) that connects $U = 0$ to a periodic orbit, then $\mathcal{H}$ must vanish along the heteroclinic orbit and on the periodic orbit. In particular, if we seek stationary fronts between the trivial state and regular hexagons, then for each fixed (μ, ν) there will typically be a unique regular hexagon, with a uniquely selected wavenumber κ, that satisfies the condition $\mathcal{H} = 0$. Under appropriate existence and transversality assumptions on the heteroclinic orbits that correspond to such fronts, we can use spatial dynamics to prove the existence of transverse homoclinic orbits, corresponding to planar hexagon pulses with the same selected hexagonal wavenumber, and of complex snaking bifurcation diagrams, and we refer to [10] for details.

For fully localized hexagon patches such as those shown in Figures 1(a) and 4, spatial dynamics may not work: while we can view the radial variable as the evolution variable, it is not clear how appropriate function spaces can be set up that allow for the increasingly finer hexagon structure in the angular variable. Nevertheless, we may formally move along the radial direction from the center of a localized hexagon patch towards infinity, and consider the interface between regular hexagons and the trivial state at the patch boundary: if this boundary becomes approximately planar as the patch grows, as seems to be the case for the hexagons patches that we present later in this paper, then we should expect, on a formal level, that the selection principle for hexagon fronts applies to localized patches too: the existence region of localized hexagon patches should therefore be centered around the Maxwell curve of the planar hexagon fronts between trivial state and regular hexagons. Furthermore, the hexagons inside the hexagon patch should satisfy $\mathcal{H} = 0$, which selects their wavenumber.

So far, we have focused on planar hexagon fronts between the trivial state and regular hexagons as these are relevant for localized hexagon patches. However, other stationary planar hexagon fronts exist, and we outline now how they arise and what their spatial profiles look like. Assume that we found a transversely constructed heteroclinic orbit of (3.7) between regular hexagons and the trivial state for the parameter values (μ_0, ν_0) and the wavenumber κ_0. If we vary the wavenumber κ near κ_0 while keeping (μ_0, ν_0) fixed, then the assumed transversality implies that the heteroclinic orbit will persist. However, this orbit will now connect the trivial state to frustrated hexagons that have minimal period $\ell = 2\pi/\kappa$ in the y-direction but are slightly compressed or expanded in the x-direction to accommodate the condition $\mathcal{H} = 0$ on the new cross-section $[0, \ell]$. The planar hexagon fronts constructed in this fashion live on the domain $\mathbb{R} \times [0, \ell]$ with periodic boundary conditions in the y-variable. Periodic boundary conditions allow us to view these fronts as planar hexagon fronts on the domains $\mathbb{R} \times [-n\ell, n\ell]$ for arbitrary positive integers n on the plane: the resulting fronts connect the trivial state to frustrated hexagon patterns that are periodic with minimal period ℓ in the transverse y-direction. The corresponding Maxwell curves will depend on ℓ (or κ), and we therefore obtain an entire family of Maxwell curves.

3.3 Regular hexagons

We prove Proposition 2 which states that, for each fixed ν, there is a unique branch of regular hexagons which bifurcate from $u = 0$ at $\mu = 0$ along which the first integral $\mathcal{H}$ from (3.2) vanishes. The wavelength of these selected hexagons may vary along the branch and therefore needs to be treated as an unknown which will adjust itself to satisfy the constraint $\mathcal{H} = 0$. This is a special case of the more general problem of finding solutions to Hamiltonian systems with prescribed Hamiltonian [9, 14, 18, 69, 75, 76]. Indeed, we prove Proposition 2 by applying the following general bifurcation theorem:

Theorem 3.1 ([9, Theorem 2.2]) *Let $\mathcal{X}$, $\mathcal{Y}$ and $\mathcal{Z}$ be Banach spaces. Let $\psi \in \mathcal{Z}^*$, $\mathcal{F} \in \mathcal{C}^\omega(\mathcal{X} \times \mathbb{R}^2, \mathcal{Y})$, and $\mathcal{H} \in \mathcal{C}^\omega(\mathcal{X} \times \mathbb{R}^2, \mathcal{Z})$, and consider the equation*

$$\begin{pmatrix} \mathcal{F}(u, \mu, \kappa) \\ \psi(\mathcal{H}(u, \mu, \kappa)) \end{pmatrix} = 0, \tag{3.9}$$

where $u \in \mathcal{X}$ and $(\mu, \kappa) \in \mathbb{R}^2$. We assume that $u = 0$ is a solution of (3.9) for all (μ, κ) with $\mathcal{H}_u(0, \mu, \kappa) \equiv 0$. Furthermore, assume that $\mathcal{F}_u(0, \mu_0, \kappa_0) \in L(\mathcal{X}, \mathcal{Y})$ is Fredholm[4] with index zero with $\mathrm{N}(\mathcal{F}_u(0, \mu_0, \kappa_0)) = \mathbb{R}\hat{u} \neq \{0\}$. We write $\mathcal{X} = \mathbb{R}\hat{u} \oplus \hat{\mathcal{X}}$, $\hat{\mathcal{Y}} := \mathrm{R}(\mathcal{F}_u(0, \mu_0, \kappa_0))$, $\mathcal{Y} = \mathbb{R}\hat{v} \oplus \hat{\mathcal{Y}}$ and denote by $P : \mathcal{Y} \to \hat{\mathcal{Y}}$ the projection along $\hat{v}$. We assume now that $\psi(\mathcal{H}_{uu}(0, \mu_0, \kappa_0)[\hat{u}, \hat{u}]) = 0$ and that the operator $D \in L(\hat{\mathcal{X}} \times \mathbb{R}^2, \hat{\mathcal{Y}} \times \mathbb{R}^2)$ given by

$$D := \begin{pmatrix} P\mathcal{F}_u(0, \mu_0, \kappa_0) & P\mathcal{F}_{u\mu}(0, \mu_0, \kappa_0)[\hat{u}, 1] & P\mathcal{F}_{u\kappa}(0, \mu_0, \kappa_0)[\hat{u}, 1] \\ 0 & (1-P)\mathcal{F}_{u\mu}(0, \mu_0, \kappa_0)[\hat{u}, 1] & (1-P)\mathcal{F}_{u\kappa}(0, \mu_0, \kappa_0)[\hat{u}, 1] \\ \psi(\mathcal{H}_{uu}[\hat{u}, \cdot]) & \psi(\mathcal{H}_{uu\mu}[\hat{u}, \hat{u}, 1]) & \psi(\mathcal{H}_{uu\kappa}[\hat{u}, \hat{u}, 1]) \end{pmatrix} \tag{3.10}$$

is an isomorphism. Under these assumptions, $(0, \mu_0, \kappa_0)$ is a bifurcation point for (3.9), and there is an interval I containing 0 and a unique analytic branch $(u, \mu, \kappa)(s)$ of solutions of (3.9), defined for $s \in I$, which satisfies $(u, \mu, \kappa)(0) = (0, \mu_0, \kappa_0)$ and $\|u(s) - s\hat{u}\|_{\mathcal{X}} = \mathrm{O}(s^2)$ as $s \to 0$.

We now set up an appropriate framework that allows us to appeal to the preceding theorem to prove Proposition 2. We first rescale (x, y) by setting $x = X/\kappa$ and $y = Y/\kappa$. In the rescaled variables, the Swift–Hohenberg equation is given by

$$(1 + \kappa^2\Delta)^2 u + \mu u - \nu u^2 + u^3 = 0.$$

We are interested in regular hexagons and therefore seek, as in §2.2, solutions with $\mathbb{D}_6$-symmetry. In addition, we require that solutions are centered at the origin to reduce the multiplicity of solutions. Thus, we set

$$\begin{aligned}
\mathcal{X} &= \Big\{ u \in \mathcal{C}^4(\mathbb{R}^2, \mathbb{R});\ u(X, Y) = u(X, Y + 4\pi/\sqrt{3}) = u(X + 2\pi, Y + 2\pi/\sqrt{3}), \\
&\qquad u(X, Y) = u((X + \sqrt{3}Y)/2, (-\sqrt{3}X + Y)/2) \quad \forall (X, Y) \Big\} \\
\mathcal{Y} &= \Big\{ u \in \mathcal{C}^0(\mathbb{R}^2, \mathbb{R});\ u(X, Y) = u(X, Y + 4\pi/\sqrt{3}) = u(X + 2\pi, Y + 2\pi/\sqrt{3}), \\
&\qquad u(X, Y) = u((X + \sqrt{3}Y)/2, (-\sqrt{3}X + Y)/2) \quad \forall (X, Y) \Big\} \\
\mathcal{Z} &= \mathcal{C}^0(\mathbb{R}, \mathbb{R})
\end{aligned}$$

and define

$$\begin{aligned}
\mathcal{F}(u, \mu, \kappa) &:= (1 + \kappa^2\Delta)^2 u + \mu u - \nu u^2 + u^3 \\
\mathcal{H}(u, \mu, \kappa) &:= \int_0^{\frac{4\pi}{\sqrt{3}}} \left[\kappa^4 \left(u_{XXX} u_X - \frac{u_{XX}^2}{2} \right) + \kappa^2 u_X^2 + \frac{(1+\mu)u^2}{2} - \frac{\nu u^3}{3} + \frac{u^4}{4} \right. \\
&\qquad \left. - \kappa^4 u_{XY}^2 - \kappa^2 u_Y^2 + \frac{\kappa^4 u_{YY}^2}{2} \right] \mathrm{d}Y \\
\psi\mathcal{H}(u, \mu, \kappa) &:= \mathcal{H}(u, \mu, \kappa)\big|_{X=0}.
\end{aligned}$$

[4] A linear operator L is called Fredholm if its null space $\mathrm{N}(L)$ is finite-dimensional, its range $\mathrm{R}(L)$ is closed, and the range $\mathrm{R}(L)$ has finite codimension. In this case, the Fredholm index is defined to be the difference $\dim \mathrm{N}(L) - \operatorname{codim} \mathrm{R}(L)$

The required regularity assumptions are then met, and it is clear that $u = 0$ is a solution for all (μ, κ) with $\mathcal{H}_u(0, \mu, \kappa) \equiv 0$. We calculate the derivatives

$$\begin{aligned}
\mathcal{F}_u(0,\mu,\kappa)[v] &= (1+\kappa^2\Delta)^2 v + \mu v \\
\mathcal{F}_{u\mu}(0,\mu,\kappa)[v] &= v \\
\mathcal{F}_{u\kappa}(0,\mu,\kappa)[v] &= 4\kappa^3\Delta^2 v + 2\kappa\Delta v \\
\mathcal{H}_{uu}(0,\mu,\kappa)[v,w] &= \int_0^{\frac{4\pi}{\sqrt{3}}} [\kappa^4(v_X w_{XXX} + v_{XXX} w_X - v_{XX} w_{XX}) + 2\kappa^2 v_X w_X + (1+\mu) vw \\
&\qquad -2\kappa^4 v_{XY} w_{XY} - 2\kappa^2 v_Y w_Y + \kappa^4 v_{YY} w_{YY}]\,\mathrm{d}Y \\
\mathcal{H}_{uu\mu}(0,\mu,\kappa)[v,w] &= \int_0^{\frac{4\pi}{\sqrt{3}}} vw\,\mathrm{d}Y \\
\mathcal{H}_{uu\kappa}(0,\mu,\kappa)[v,w] &= \int_0^{\frac{4\pi}{\sqrt{3}}} [4\kappa^3(v_X w_{XXX} + v_{XXX} w_X - v_{XX} w_{XX}) + 4\kappa v_X w_X \\
&\qquad -8\kappa^3 v_{XY} w_{XY} - 4\kappa v_Y w_Y + 4\kappa^3 v_{YY} w_{YY}]\,\mathrm{d}Y.
\end{aligned}$$

The analysis reviewed in §2.2 implies that we should pick $(\mu_0, \kappa_0) = (0, 1)$ for which $\mathcal{F}_u(0, 0, 1)$ has a one-dimensional null space spanned by

$$\hat{u}(X, Y) = \cos(X) + \cos((X + \sqrt{3}Y)/2) + \cos((X - \sqrt{3}Y)/2).$$

We may set $\hat{v} := \hat{u}$ and use the L^2-inner product on the fundamental periodicity domain $[0, 4\pi] \times [0, 4\pi/\sqrt{3}]$ to define complements $\hat{\mathcal{X}}$ and $\hat{\mathcal{Y}}$ of $\mathbb{R}\hat{u}$ in $\mathcal{X}$ and $\mathcal{Y}$, as $\mathcal{F}_u(0, 0, 1)$ is symmetric with respect to this inner product.

Substituting these expressions, we find that $\mathcal{H}_{uu}(0, 0, 1)[\hat{u}, \hat{u}] = 0$. Furthermore, we find that the operator D defined in (3.10) is given by

$$D = \begin{pmatrix} P\mathcal{F}_u(0,0,1) & 0 & 0 \\ 0 & 1 & 2 \\ \star & 4\pi\sqrt{3} & -8\pi\sqrt{3} \end{pmatrix} \in L(\hat{\mathcal{X}} \times \mathbb{R}^2, \hat{\mathcal{Y}} \times \mathbb{R}^2).$$

In particular, this operator is invertible, and we obtain the following result, which is formulated again in the original spatial variables:

Proposition 3 ($\mathcal{L}$-periodic hexagons with $\mathcal{H} = 0$) *Fix any ν, then there exists an interval $I \subset \mathbb{R}$ and a unique branch $s \mapsto (u, \mu, \kappa)(s)$ of nontrivial $\mathcal{L}$-periodic hexagons of the Swift–Hohenberg equation (3.1) with zero constraint (3.8) and aspect ratio $\kappa(s)$, which are defined and smooth for $s \in I$. Moreover, $(u, \mu, \kappa)(0) = (0, 0, 1)$ and*

$$\Big\| [u(s)](x,y) - s\left[\cos(\kappa(s)x) + \cos(\kappa(s)(x+\sqrt{3}y)/2) + \cos(\kappa(s)(x-\sqrt{3}y)/2)\right] \Big\|_{C^4} = \mathrm{O}(s^2) \tag{3.11}$$

as $s \to 0$.

For $\nu > 0$, (2.7) and (3.11) imply that $\mu(s) > 0$ for all sufficiently small $s > 0$, as claimed in Proposition 2.

4 Numerical algorithms

In this section, we describe the numerical algorithms, and their implementation, that we used to compute regular hexagons, planar hexagon pulses, and localized hexagon patches.

Though we will rely on continuation methods for most of our computations, we shall also occasionally employ an initial value problem solver, which we discuss first. Afterwards, we outline the computation of regular hexagons and the associated hexagon Maxwell curve. This information will guide us as to where we may

find hexagon pulses and localized hexagon structures in the Swift–Hohenberg equation. We then move on to the computation of planar hexagon pulses that are periodic in the transverse direction. Last, we present the numerical methods for the computation of localized hexagon patches: these methods are designed to take advantage of the $\mathbb{D}_6$-symmetry of localized structures and allow us to compute localized structures that extend over large spatial regions. The computations of localized hexagon patches were also repeated with other methods to check the reliability of the numerical results.

The actual computations were carried out on FINCH, a dual core 2.7 GHz PowerPC G5 with 4GB of RAM, and PHOENIX, a server with two 3GHz dual core Xeon processors with 8GB of RAM, both running Mac OS 10.4.

4.1 The initial value problem solver

To quickly find solutions of the Swift–Hohenberg equation, investigate the stability of patterns with respect to small symmetry-breaking perturbations, and confirm the solutions obtained from our other numerical solvers, we employ an initial value problem solver for the Swift–Hohenberg equation (1.1), which we shall now discuss briefly. First, we use the 2D Fourier transform to reduce the initial value problem on a rectangular box with periodic boundary conditions to a system of ODEs. The resulting ODE system is truncated at a sufficiently large Fourier mode and solved in time using the first-order exponential time-stepping algorithm developed in [27]. We implemented this solver in MATLAB. Computations are done on domains of size 60×60 with 256×256 and 512×512 Fourier modes. Typical time steps are 0.01 and 0.001.

4.2 Regular hexagons and Maxwell curves

To find regular hexagons, we proceed initially as in §3.3. It has been shown in [61, 62] that regular hexagons can be computed in a rectangular box with Neumann boundary conditions provided the ratio of the lengths of the sides of the rectangle is an integer multiple of $\sqrt{3}$. Thus, we introduce new independent coordinates $X = \kappa x$ and $Y = \kappa y$ and use the rescaled Swift–Hohenberg equation

$$\mathcal{F}(u;\mu,\nu,\kappa) = (1+\kappa^2\Delta)^2 u + \mu u - \nu u^2 + u^3 = 0, \qquad (X,Y) \in \Omega_{\text{hex}} \tag{4.1}$$

on the computational domain $\Omega_{\text{hex}} = (0, 4\pi) \times (0, 4\pi/\sqrt{3})$ with Neumann boundary conditions; see Figure 13(a).

For the computation of Maxwell curves, we add the constraints

$$\mathcal{H}(u;\mu,\nu,\kappa) = \int_0^{\frac{4\pi}{\sqrt{3}}} \left[-\frac{\kappa^4 (u_{XX})^2}{2} + \frac{(1+\mu)u^2}{2} - \frac{\nu u^3}{3} + \frac{u^4}{4} - \kappa^2 (u_Y)^2 + \frac{\kappa^4 (u_{YY})^2}{2} \right]_{X=0} \mathrm{d}Y = 0, \tag{4.2}$$

which ensures that the first integral $\mathcal{H}$ vanishes, and

$$\mathcal{E}(u;\mu,\nu,\kappa) = \int_{\Omega_{\text{hex}}} \left[\frac{[(1+\kappa^2\Delta)u]^2}{2} + \frac{\mu u^2}{2} - \frac{\nu u^3}{3} + \frac{u^4}{4} \right] \mathrm{d}X\,\mathrm{d}Y = 0, \tag{4.3}$$

which enforces zero energy. Note that several terms in the original expression (3.2) for $\mathcal{H}$ vanish on account of the Neumann conditions $u_X(0,Y) = u_{XXX}(0,Y) = 0$. The choice of our computational domain means that we accurately compute the energy of two full hexagons in (4.3); see Figure 13(a).

We expect that the equation $\mathcal{F}(u;\mu,\nu,\kappa) = 0$ has a locally unique regular zero u for each fixed (μ,ν,κ) in appropriate regions[5] in parameter space. We can also use (4.1) together with the constraints (4.2)-(4.3) in a numerical continuation framework where we expect to find a curve of solutions (u,μ,ν,κ) that depend on a one-dimensional arclength parameter s. Since the resulting Maxwell curves do not exhibit any folds in the parameter μ, we can, in fact, compute this curve by stepping in the parameter μ.

For the actual computations, we evaluate derivatives using spectral differentiation as in [87, §3] and compute the integrals in the constraints (4.2)-(4.3) using the periodic trapezoid rule [87, §12]. We now briefly outline

[5] For instance, for μ close to zero due to the results in §2.2; see also Proposition 3

how this is done in our context. We choose the mesh $X_i = 4\pi i/N$ and $Y_j = 4\pi j/N\sqrt{3}$ for $i, j = 1, \dots N$ and write $u_{ij} = u(X_i, Y_j)$ on this mesh. A convenient way for evaluating first-order derivatives and the Laplacian is via Kronecker products: if A is an $m \times n$ matrix and B is a $p \times q$ matrix, then the Kronecker product $A \otimes B$ is an $mp \times nq$ matrix which consists of $m \times n$ blocks where each block is a $p \times q$ matrix: the (i, j)th block is given by $a_{ij}B$. Introducing the step size $h = 2\pi/N$, the spectral differentiation matrices for functions of one variable are given by

$$D_N = \text{toeplitz}\left[0,\ \left(\frac{(-1)^j}{2\tan(jh/2)}\right)_{j=1,\dots,N-1}\right]$$

for the first derivative and by

$$D_N^{(2)} = \text{toeplitz}\left[-\frac{\pi^2}{3h^2} - \frac{1}{6},\ \left(-\frac{(-1)^j}{2\sin^2(jh/2)}\right)_{j=1,\dots,N-1}\right]$$

for the second derivative [87, §3], where toeplitz[v] denotes the symmetric Toeplitz matrix (a matrix whose entries are constant along each diagonal) formed by the row vector $v \in \mathbb{R}^N$. Using Kronecker products, we can now set up the $N^2 \times N^2$ differentiation matrices for $u(X, Y)$ which are given by

$$D_{X,N} = I \otimes \left(\frac{1}{4}\right) D_N, \qquad D_{Y,N} = \left(\frac{\sqrt{3}}{4}\right) D_N \otimes I, \qquad \Delta_N = I \otimes \left(\frac{1}{4}\right)^2 D_N^{(2)} + \left(\frac{\sqrt{3}}{4}\right)^2 D_N^{(2)} \otimes I$$

corresponding, respectively, to the first-order derivatives ∂_X and ∂_Y and to the Laplacian Δ.

The above procedure results in a finite-dimensional system. We solve this system in MATLAB using the nonlinear Newton trust-region solver FSOLVE. For (μ, ν) close to zero, we choose

$$u(X, Y) = A[\cos(X) + \cos((X + \sqrt{3}Y)/2) + \cos((X - \sqrt{3}Y)/2)]$$

as an initial guess, where a good approximation for the amplitude A can be obtained from normal-form theory by solving (2.7). MATLAB's Newton trust-region solver has the advantage of often achieving global convergence even when starting from poor initial guesses. We have frequently obtained better convergence by solving initially only the Swift–Hohenberg equation, without the integral constraints (4.2)-(4.3), with $\kappa = 1$ and ν fixed. Afterwards, using this solution as initial data, we solve the Swift–Hohenberg equation together with one or both of the integral constraints by including one or two of the parameters κ and ν as unknowns. Once we have a solution to (4.1)-(4.3), we continue it in μ by stepping in the parameter μ and solving (4.1)-(4.3) for (u, ν, κ) for each fixed μ. We use $18 \cdot 18 = 324$ interpolation points in the box $\Omega_{\text{hex}} = (0, 4\pi) \times (0, \frac{4\pi}{\sqrt{3}})$ and compute solutions within an absolute tolerance of 10^{-4}. The entire Maxwell curve was computed in a couple of minutes.

4.3 Numerical continuation of planar hexagon pulses

In this section, we discuss the computation of stationary planar hexagon pulses with Bravais–Miller indices $\langle 10 \rangle$ and $\langle 11 \rangle$ such as those shown in Figure 3. The interfaces in these solutions are vertical, and the overall patterns are periodic in the transverse y-direction and reflection symmetric.

Hence, we will focus on computing stationary solutions $u(x, y)$ of the planar Swift–Hohenberg equation that are periodic in the y-direction and are symmetric under reflections in x and y so that $u(-x, y) = u(x, y) = u(x, -y)$ for all (x, y). These solutions therefore satisfy

$$(1 + \Delta)^2 u + \mu u - \nu u^2 + u^3 = 0, \qquad (x, y) \in \Omega \tag{4.4}$$

on $\Omega = (0, \ell_x) \times (0, \ell_y)$ with Neumann boundary conditions

$$u_x|_{\{x=0,\ell_x\}} = u_{xxx}|_{\{x=0,\ell_x\}} = u_y|_{\{y=0,\ell_y\}} = u_{yyy}|_{\{y=0,\ell_y\}} = 0 \tag{4.5}$$

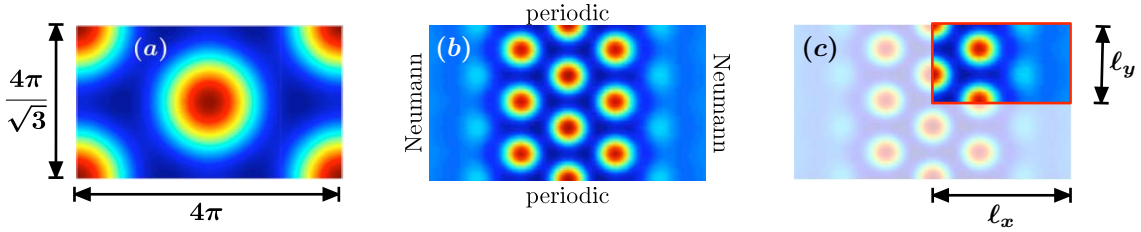

Figure 13: *Regular hexagons are computed with Neumann boundary conditions on the domain* Ω_{hex} *shown in panel (a). Reflection-symmetric planar hexagon pulses are defined on the domain shown in panel (b) with Neumann conditions in the horizontal* x*-direction and periodic boundary conditions in the vertical* y*-direction. Panel (c) illustrates the computational domain* $\Omega = (0, \ell_x) \times (0, \ell_y)$ *with Neumann conditions.*

on $\partial\Omega$, see Figure 13. We need to choose ℓ_x large enough to avoid boundary effects (we used $\ell_x = 50$), while ℓ_y is chosen in such a way as to accommodate hexagon interfaces with $\langle 10 \rangle$ or $\langle 11 \rangle$ orientation: we pick $\ell_y = 4\pi n/\sqrt{3}$ for interfaces with index $\langle 10 \rangle$ and $\ell_y = 2\pi n$ for interfaces with index $\langle 11 \rangle$. The choice of $n \in \mathbb{N}$ allows us to compute patterns for several wavelengths in the vertical y-direction.

Fixing the length ℓ_y of the domain in the y-direction may frustrate the hexagons: since regular hexagons can no longer choose their wavenumber freely to satisfy the constraint $\mathcal{H} = 0$, the patterned state will typically consist of frustrated hexagons that have a fixed period ℓ_y/N in the y-variable for some integer N to accommodate the fixed length in the y-direction, while their wavelength in the x-direction adjusts itself to satisfy the constraint $\mathcal{H} = 0$; the resulting frustrated hexagons are therefore slightly compressed or elongated in the x-direction and no longer $\mathbb{D}_6$-symmetric. We could add the constraint (4.2) and allow ℓ_y to vary so that regular hexagons always fit into the domain. Since we have found that the regular hexagons for which $\mathcal{H} = 0$ have wavenumbers κ very close to $\kappa = 1$, we believe that the effect of fixing ℓ_y on the selected patterns is negligible. However, the snaking limits of the planar hexagon pulses may coincide better with the snaking limits of the localized hexagon patches had we elected to allow ℓ_y to vary.

To solve (4.4)-(4.5) numerically, we used a 13-point finite difference stencil for the spatial discretization. We implemented the resulting system in the continuation framework PARACONT [7], a module built on top of the continuation module LOCA of the package TRILINOS which is written and maintained by Sandia Laboratories [43]. Since TRILINOS does not currently offer a direct solver for LOCA that works on parallel processors, we employed a multi-level preconditioner on a coarse level so that an exact sparse linear solve is done. The computations were carried out on the domain $\Omega = (0, \ell_x) \times (0, \ell_y)$ with $\ell_x = 50$. We used $\ell_y = 20\pi/\sqrt{3}$ for $\langle 10 \rangle$ pulses and $\ell_y = 10\pi$ for $\langle 11 \rangle$ pulses, and worked with both 128×256 and 256×256 mesh points for both computations.

We remark that localized pulses on long cylinders $(0, \ell_x) \times S^1$ have been computed previously in the von Karman–Donnell equations, a coupled system of elliptic PDEs that describe equilibria of axially compressed cylindrical shells [46, 59]. The approach adopted there was to carry out a Fourier decomposition in the angular direction leading to a large system of ordinary differential equations that were solved with the boundary-value solver AUTO97.

4.4 Numerical continuation of localized hexagon patches

We now turn to the computation and continuation of planar localized hexagon patches such as the ones presented in Figures 1(a) and 4. We focus on the computation of patterns with $\mathbb{D}_6$-symmetry. Since we found that sparse Cartesian meshes give a preference to $\mathbb{D}_4$-symmetric square patterns, we discretize the planar Swift–Hohenberg equation in polar coordinates. In particular, we found that a spectral Fourier discretization in the angular coordinate combined with an adaptive collocation mesh in the radial coordinate appears to be a very efficient method for computing localized hexagon patches.

In the following, we will outline our approach for computing localized patterns with an arbitrary $\mathbb{D}_{2k}$-

symmetry[6]. Restricting ourselves to solutions with $\mathbb{D}_{2k}$-symmetry allows us to compute them on the first quadrant $\Omega = \{x, y > 0\}$ with Neumann boundary conditions which is advantageous for various reasons. First, it factors out, in a natural fashion and without the need of introducing additional constraints, the continuous translation and rotation symmetries in $\mathbb{E}(2)$ of the Swift–Hohenberg equation whose presence would otherwise yield a singular Jacobian which is problematic for Newton solvers. Second, computing solely on the first quadrant greatly reduces the size of the discretized system. Third, as already mentioned, we can center localized solutions at the origin and compute efficiently in polar coordinates. The main disadvantage of computing on the first quadrant is that temporal stability cannot be deduced and bifurcations to $\mathbb{D}_{2k+1}$ patterns cannot be detected. Overall, we believe that the advantages outweigh the disadvantage of potentially failing to detect instabilities during continuation as these can often be identified a posteriori by direct numerical simulations.

We therefore consider the stationary planar Swift–Hohenberg equation

$$(1 + \Delta_{r,\theta})^2 u + \mu u - \nu u^2 + u^3 = 0 \tag{4.6}$$

written in polar coordinates $(r, \theta) \in (0, \infty) \times [0, 2\pi)$ where

$$\Delta_{r,\theta} u = u_{rr} + \frac{u_r}{r} + \frac{u_{\theta\theta}}{r^2}.$$

Polar coordinates are singular at $r = 0$, and we need to find appropriate boundary conditions at the origin to remove this singularity. To do this, we follow [84]. Assuming that u is a sufficiently localized solution, we multiply (4.6) by another localized function v and subsequently integrate over (r, θ) to arrive at the weak formulation

$$\begin{aligned} &\int_0^{2\pi} \int_0^{\infty} \left[\Delta u \Delta v - 2\nabla u \nabla v + (1+\mu) uv - \nu u^2 v + u^3 v\right] r \,\mathrm{d}r \,\mathrm{d}\theta \\ &= \int_0^{2\pi} \int_0^{\infty} \left[\left(\frac{(ru_r)_r}{r} + \frac{u_{\theta\theta}}{r^2} \right) \left(\frac{(rv_r)_r}{r} + \frac{v_{\theta\theta}}{r^2} \right) - 2 \left(u_r v_r + \frac{u_\theta v_\theta}{r^2} \right) + (1+\mu) uv - \nu u^2 v + u^3 v \right] r \,\mathrm{d}r \,\mathrm{d}\theta = 0 \end{aligned} \tag{4.7}$$

of (4.6). The boundary conditions at $r = 0$ which make the bilinear form (4.7) meaningful are

$$u_r|_{(0,\theta)} = (ru_r)_r|_{(0,\theta)} = u_\theta|_{(0,\theta)} = u_{\theta r}|_{(0,\theta)} = u_{\theta\theta}|_{(0,\theta)} = (u_{\theta\theta})_r|_{(0,\theta)} = 0 \qquad \forall \theta \in [0, 2\pi).$$

Since $(ru_r)_r = ru_{rr} + u_r$, the conditions above reduce to

$$u_r(0, \theta) = u_{\theta\theta}(0, \theta) = u_{\theta\theta r}(0, \theta) = 0 \qquad \forall \theta \in [0, 2\pi). \tag{4.8}$$

We now expand $u(r, \theta)$ in a Fourier series which we truncate at order $N \in \mathbb{N}$ to get a finite-dimensional system. Thus, we set

$$u(r, \theta) = \sum_{n=-N}^{N} a_n(r) \mathrm{e}^{-\mathrm{i}n\theta}, \tag{4.9}$$

where N is the truncation order, and $a_n(r)$ is complex-valued for each n. The Laplacian becomes

$$\Delta_{r,\theta} u = \sum_{n=-N}^{N} \left[\partial_r^2 a_n + \frac{\partial_r a_n}{r} - \frac{n^2 a_n}{r^2} \right] \mathrm{e}^{-\mathrm{i}n\theta}.$$

Substituting these expressions, we find that the truncated planar Swift–Hohenberg equation (4.6) can be written as

$$\begin{aligned} &\partial_r^4 a_n + \frac{2\partial_r^3 a_n}{r} - \frac{\partial_r^2 a_n}{r^2} + \frac{\partial_r a_n}{r^3} - \frac{2n^2 \partial_r^2 a_n}{r^2} + \frac{2n^2 \partial_r a_n}{r^3} - \frac{4n^2 a_n}{r^4} + \frac{n^4 a_n}{r^4} \\ &\quad + 2 \left(\partial_r^2 a_n + \frac{\partial_r a_n}{r} - \frac{n^2 a_n}{r^2} \right) + (1+\mu) a_n - \nu \sum_{p+q=n} a_p a_q + \sum_{p+q+s=n} a_p a_q a_s = 0, \end{aligned} \tag{4.10}$$

[6]This method can be extended to localized $\mathbb{D}_{2k+1}$-symmetric patterns but we do not go into the details here

while the boundary conditions (4.8) at the origin reduce to

$$\begin{aligned} \partial_r a_0\big|_{r=0} &= \partial_r^3 a_0\big|_{r=0} = 0 \\ a_n\big|_{r=0} &= \partial_r a_n\big|_{r=0} = 0 \qquad \forall n \neq 0. \end{aligned}$$

Solutions $u(r,\theta)$ with $\mathbb{D}_{2k}$ symmetry are invariant under the reflection $\theta \mapsto -\theta$ and the rotation $\theta \mapsto \theta - \pi$ so that

$$u(r,\theta) = u(r,-\theta) \quad \text{and} \quad u(r,\theta) = u(r,\theta-\pi)$$

for all (r,θ). These identities imply that

$$a_n = a_{-n} \quad \text{and} \quad a_n = (-1)^n a_n \quad \forall n$$

for the coefficients $a_n(r)$ of the Fourier representation (4.9) of u. The first of these two conditions implies that we need to compute the coefficients a_n only for $n \geq 0$, while the second condition implies that all odd Fourier coefficients a_{2n+1} must vanish identically. The two summations in (4.10) can then be simplified by noting that

$$\begin{aligned} \sum_{p+q=n} a_p a_q &= \sum_{p=-N}^{N} a_{|p|} a_{|n-p|} \\ \sum_{p+q+s=n} a_p a_q a_s &= \sum_{p=-N}^{N} \sum_{q=-N}^{N} a_{|p|} a_{|q|} a_{|n-p-q|}. \end{aligned}$$

So far, we have considered solutions with an arbitrary $\mathbb{D}_{2k}$-symmetry. From now on, we restrict ourselves to solutions with $\mathbb{D}_6$-symmetry such as hexagons. Such solutions are in addition invariant under rotations by an angle of $\pi/3$, which is equivalent to requiring that

$$a_n = \mathrm{e}^{\mathrm{i}n\pi/3} a_n \qquad \forall n.$$

The only nonzero modes that can satisfy this constraint are those for which $n = 6m$ for some $m \in \mathbb{Z}$. Hence, for the purpose of computing localized $\mathbb{D}_6$-symmetric solutions, we need to consider only the Fourier modes $a_{6m}(r)$: note that the space spanned by these modes is the fixed-point space under the $\mathbb{D}_6$-action, and therefore invariant under the evolution of (4.10). Thus, we set

$$A_m(r) := a_{6m}(r) \qquad |m| \leq M$$

with $N = 6M$ and write (4.10) as the first-order system

$$\begin{aligned} \partial_r A_m &= B_m \\ \partial_r B_m &= C_m \\ \partial_r C_m &= D_m \\ \partial_r D_m &= -\frac{2D_m}{r} + \frac{C_m}{r^2} - \frac{B_m}{r^3} + \frac{2(6m)^2 C_m}{r^2} - \frac{2(6m)^2 B_m}{r^3} + \frac{4(6m)^2 A_m}{r^4} - \frac{(6m)^4 A_m}{r^4} \\ &\quad -2\left(C_m + \frac{B_m}{r} - \frac{(6m)^2 A_m}{r^2}\right) - (1+\mu) A_m \\ &\quad +\nu \sum_{p=-M}^{M} A_{|p|} A_{|m-p|} - \sum_{p=-M}^{M} \sum_{q=-M}^{M} A_{|p|} A_{|q|} A_{|m-p-q|} \end{aligned} \tag{4.11}$$

with boundary conditions

$$\begin{aligned} \partial_r A_0\big|_{r=0} &= D_0\big|_{r=0} = 0 \\ A_m\big|_{r=0} &= C_m\big|_{r=0} = 0 \qquad \forall m \neq 0 \\ A_m\big|_{r=R} &= B_m\big|_{r=R} = 0 \qquad \forall m \end{aligned} \tag{4.12}$$

where R indicates the radial domain $(0, R)$ on which we compute solutions.

Both the domain truncation parameter R and the Fourier truncation parameter M must be set to suitably large values to ensure that the Neumann boundary conditions at $r = R$ do not influence the localized patterns and to make sure that the Fourier modes can resolve the angular dependence of the computed patterns. Close to $(\mu, \nu) = 0$, the localized patterns are small in amplitude but are also well spread out: this requires both R and M to be large. Specifically, we expect that the number of Fourier modes required to resolve a localized hexagon patch corresponds roughly to the number of hexagon rings one wishes to interpolate: if we wish to compute a hexagon patch of radius R, then it will have approximately R hexagons, or more, located on its interface. To resolve these R hexagons, we need at least $M \approx R$ Fourier modes in the angular variable, and this is indeed what we find in our numerical computations.

A major problem is acquiring good initial data for continuation. We use two different methods for preparing good initial guesses for the boundary-value problem (4.11)-(4.12). The first method is to use an initial value problem solver and find a stable stationary localized hexagon patch by direct numerical simulations: as we can first compute the Maxwell curve, we do know where to look for stable hexagon patches. Our experience was, however, that convergence to stationary solutions tends to be very slow. Instead, we have found that it is better to discretize the boundary-value problem (4.11)-(4.12) in the radial variable using a Chebyshev decomposition with an infinite mapping in the radial coordinate r that bunches the collocation points near the origin as in [57]. We then use MATLAB's Newton trust-region solver FSOLVE starting from initial data of the form

$$u(x, y) = a\ \mathrm{sech}(b\sqrt{x^2 + y^2}) \left[\cos(x) + \cos((x + \sqrt{3}y)/2) + \cos((x - \sqrt{3}y)/2)\right],$$

where a is chosen to be close to or greater than the maximum height of a single hexagon cell and b determines the size of the localized hexagon patch. This procedure gives excellent convergence results and allowed us to obtain accurate starting data for subsequent continuation in parameters.

As already mentioned, initial data for hexagon patches were computed using MATLAB's Newton trust-region solver. To continue these solutions, we implemented the boundary-value problem (4.11)-(4.12) in AUTO07P [34]. Within AUTO07P, we computed the L^2-norm of solutions by appending an additional equation together with another parameter that corresponds to the value of the L^2-norm of a solution; we exclude this additional equation from the calculation of the pseudo-arclength. The Jacobian of the right-hand side of (4.11) was supplied in analytic form to speed up the computation. We use standard AUTO07P tolerances and choose the collocation mesh size NTST between 200 and 400. The radial domain truncation parameter R was set to $R = 80, 100, 200$, while the number of angular Fourier modes is taken to be $M = 20, 30, 40$. The computation of the full hexagon snake took up to one day on PHOENIX.

Hexagon patches have been computed previously in [63] in the context of nonlinear optics. In fact, the authors there computed and continued several different localized states and traced out the beginning of the snaking diagram. They discretized the underlying PDE on an equidistant mesh, used the fast Fourier transform for evaluating the spatial derivatives, and solved the resulting large system of algebraic equations using Newton's method. This method tends to be computationally expensive (their computations required the use of 300 servers with 500MHz processors) since the mesh requires a large number of modes even in the tails of the localized pattern.

5 Localized hexagon and rhomboid patches: Numerical results

In this section, we present our numerical results. We emphasize that the computational domains of numerical solutions are typically much larger than the domains visible in the figures presented below as we frequently cropped images to highlight the features of the localized patterns.

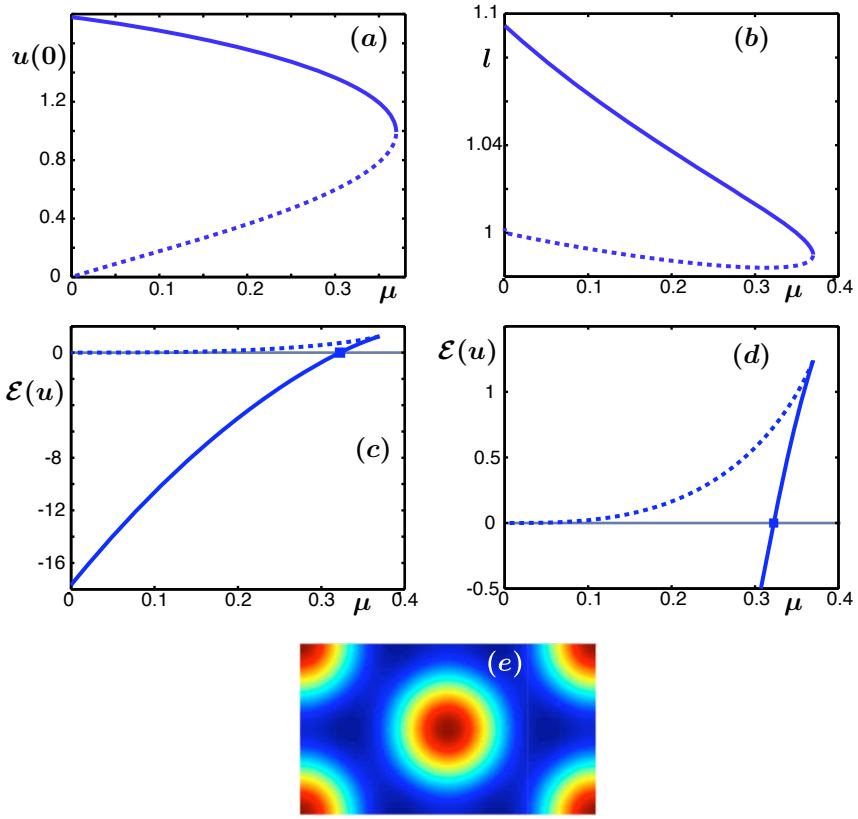

Figure 14: *We computed regular hexagons with $\mathcal{H} = 0$ as solutions of (4.1)-(4.2) with $\nu = 1.6$. Stable hexagons are plotted in solid lines, unstable ones in dashed lines. We plot the amplitude $u(0,0)$ at the origin in panel (a), the wavelength $l = 1/\kappa$ of the hexagons in (b), and the energy $\mathcal{E}(u)$ along the branch in (c)-(d). The Maxwell point $\mathcal{E}(u) = 0$ occurs at $\mu = \mu_{\rm M} = 0.3224$ on the stable branch. Compared with the trivial state, stable regular hexagons have less energy to the left and higher energy to the right of the Maxwell point. Panel (e) contains a color plot of the regular hexagons $u(x, y)$ on the domain $[0, 4\pi l] \times [0, 4\pi l/\sqrt{3}]$ at the Maxwell point.*

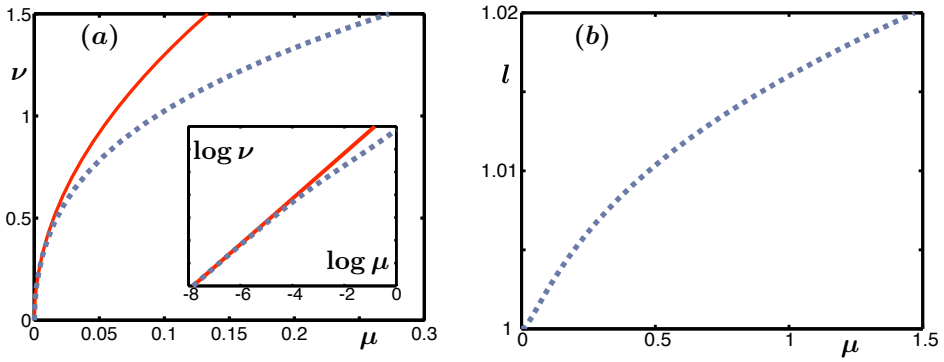

Figure 15: *In panel (a), we plot the Maxwell curve along which the regular hexagons of (4.1) satisfy the constraints $\mathcal{H} = 0$ and $\mathcal{E} = 0$ from (4.2) and (4.3), respectively: the numerical result is dashed, while the analytic prediction $\mu = \mu_{\rm M} = 8\nu^2/135$, valid in the limit $\nu \to 0$, is plotted as a solid line. Panel (b) gives the wavelength $l = 1/\kappa$ of the corresponding hexagons.*

5.1 Regular hexagons and Maxwell curves

We first compute regular hexagons of the planar Swift–Hohenberg equation that satisfy $\mathcal{H} = 0$ as solutions to (4.1)-(4.2) with $\nu = 1.6$. As discussed in §3, only these hexagons can be connected to the trivial state by a stationary planar front. The bifurcation diagram shown in Figure 14(a) is qualitatively similar to that found in §2.2 in the normal-form analysis for $|\nu| \ll 1$: regular hexagons bifurcate off the trivial solution at $\mu = 0$ and are initially unstable but regain stability in a saddle-node bifurcation. Figure 14(b) contains a plot of the wavelength $l := 1/\kappa$ of the hexagons with $\mathcal{H} = 0$ as μ is varied. The energy $\mathcal{E}(u)$ of these hexagons, computed over two hexagons, is shown in Figure 14(c)-(d) as a function of μ. In particular, the Maxwell point, where $\mathcal{E} = 0$, occurs at $\mu = \mu_{\mathrm{M}} = 0.3224$, and we plot the computed hexagon at the Maxwell point in Figure 14(e). We remark that the dependence of the wavelength and the energy on the parameter μ is qualitatively similar for hexagons and 1D rolls; see Figure 5(iii)-(iv) or [19, Figure 2] for results on rolls.

Next, we solve (4.1)-(4.3) for (u, μ, ν, κ) which gives the hexagon Maxwell curve along which hexagons with zero energy $\mathcal{E} = 0$ and zero first integral $\mathcal{H} = 0$ exist. As discussed in §3, this curve serves as a guide to where hexagon fronts and pulses as well as fully localized hexagon patches can be expected. In Figure 15, we plot both the hexagon Maxwell curve in (μ, ν)-parameter space and the dependence of the wavelength $l = 1/\kappa$ of the selected hexagons on the parameter μ. As predicted by the theory outlined in §2.3, the Maxwell curve emerges from the codimension-two point $(\mu, \nu) = (0, 0)$ and agrees well with the analytic prediction $\mu_{\mathrm{M}} = 8\nu^2/135$ given in (2.12). The wavelength of the hexagons increases along the Maxwell curve. We remark that, for $0 \leq \mu \leq 0.6$, the Maxwell curve agrees well with the curve obtained from setting $\mathcal{E} = 0$ and allowing arbitrary values for $\mathcal{H}$ while keeping $\kappa = 1$ fixed (we do not show a comparison of these curves though).

As shown in Figure 14(d), stable regular hexagons have less energy than the trivial state to the left of the Maxwell curve and higher energy to its right. Thus, we expect that hexagons will invade the trivial state for μ sufficiently far to the left of the Maxwell curve, while the trivial state will invade hexagons for μ sufficiently far to its right.

5.2 Planar hexagon pulses: Bifurcation diagram for $\nu = 1.6$

Throughout this section, we fix $\nu = 1.6$ and recall that the hexagon Maxwell point is given by $\mu = 0.3224$.

We compute planar hexagon pulses of the Swift–Hohenberg equation with Bravais–Miller indices $\langle 10 \rangle$ and $\langle 11 \rangle$. Example plots of these solutions for $\mu = 0.31$ are given in Figure 3. Since we fixed the computational domain in these computations, all hexagons are slightly compressed by the same fraction in the y-direction instead of being fully $\mathbb{D}_6$-symmetric: each vertical slice $u(x, \cdot)$ of the planar hexagon pulse $u(x, y)$ must satisfy $\mathcal{H} = 0$ for each x, and since regular hexagons cannot adjust their wavelength in the y-direction to

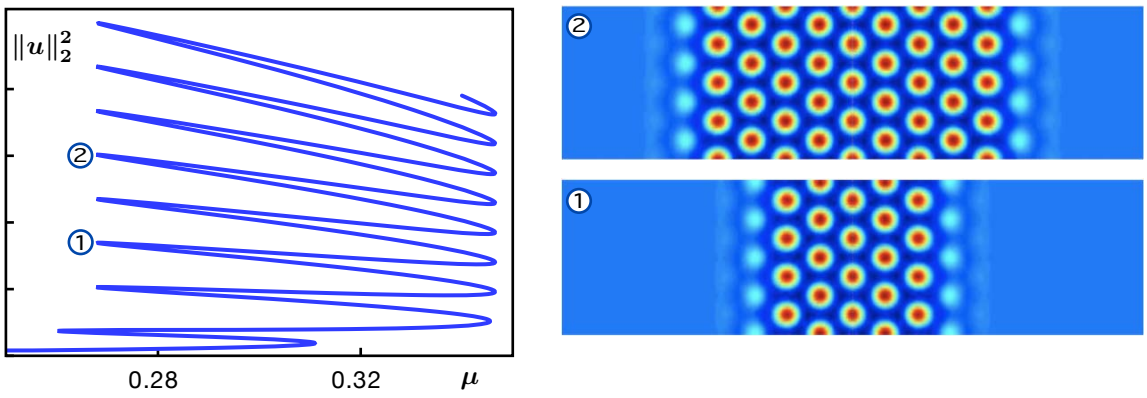

Figure 16: *The left panel contains the bifurcation diagram of planar* $\langle 10 \rangle$ *hexagon pulses, while two selected profiles at the labelled parameter values are shown in the right two panels.*

accommodate this condition due to the fixed domain dimension, the selected patterns are slightly frustrated hexagons. The frustrated hexagons are still periodic in both the x- and the y-direction but their wavelengths in the x- and y-direction are no longer in a $\sqrt{3}:1$ ratio as those of regular hexagons.

Upon varying μ, we find that planar $\langle 10\rangle$ hexagon pulses snake as shown in Figure 16. Upon passing through a pair of fold bifurcations, the pulses acquire an additional full column of hexagons and thereby widen in the horizontal x-direction. As outlined in §3.2, we can consider the planar Swift–Hohenberg equation as a dynamical system in an unbounded direction provided we restrict ourselves to a bounded cross-section in the remaining spatial variable. To explain the snaking of planar $\langle 10\rangle$ pulses, we treat the x-variable as our time-like variable and restrict y to a bounded interval with Neumann boundary conditions. As can be seen from Figure 17(i), a planar hexagon pulse corresponds to a homoclinic orbit of the trivial state $U = 0$ which passes close to a periodic orbit in the x-dynamics that is formed of hexagons. Thus, we are in the situation discussed in §2.1 and §3.2 and expect snaking to set in [10]. As already alluded to in §3.2, the scenario we just described persists if we change the height of the y-interval: the selected hexagons will become slightly frustrated and, accordingly, the Maxwell point may change slightly, but the resulting planar hexagon pulses will continue to snake.

As shown in Figure 18(a), planar $\langle 10\rangle$ pulses undergo additional pitchfork bifurcations near each fold. Figure 18(b)-(c) shows that the patterns bifurcating at the pitchfork bifurcations are almost-planar hexagon pulses: at onset, either one or two hexagon cells appear in new columns to the left and right at the center of the $\langle 10\rangle$ pulse. As we move along the bifurcating branch, the almost-planar hexagon pulses begin to snake and, at each fold, additional pairs of hexagon cells are added symmetrically above and below the already added hexagon cells until the entire column is filled. At this point, the branch of almost planar pulses terminates in a second pitchfork bifurcation at the planar $\langle 10\rangle$ hexagon pulses. Almost-planar hexagon pulses undergo only a finite number of folds due to the finite height of the computational domain. Similar to the case of planar pulses, the left and right fold bifurcations of almost-planar hexagon pulses line up. To explain the snaking of almost planar pulses, we consider the y-variable as our time-like variable and restrict x to a large bounded interval with Neumann boundary conditions; see Figure 17(ii). In this spatial-dynamics interpretation, an almost-planar hexagon pulse corresponds to a homoclinic orbit of a periodic orbit that passes close to a second periodic orbits as y increases. Each periodic orbit in the y-dynamics consists of a localized hexagon pulse in the x-variable with a different number of hexagons in its center. Homoclinic orbits between periodic orbits will snake in the same fashion as the homoclinic orbits between equilibria that we discussed in §2.1.

We now turn to a discussion of planar $\langle 11\rangle$ hexagon pulses which also snake, see Figure 19, and exhibit pitchfork bifurcation to almost planar $\langle 11\rangle$ pulses as shown in Figure 20. The almost-planar $\langle 11\rangle$ hexagon pulses undergo only two folds since the computational domain allows only eight hexagons in the y-direction: there would be more folds if the height ℓ_y of the computational domain used in Figure 13 was larger.

Figure 21 contains the bifurcation diagrams of both planar $\langle 10\rangle$ and $\langle 11\rangle$ hexagon pulses. This figure shows that the orientation of the hexagon pulse has a significant effect on the width of the snaking region. The different vertical lines along which the folds line up will play an important role later when we discuss fully localized hexagon patches. We believe that there are many other hexagon pulses with orientations different from $\langle 10\rangle$ and $\langle 11\rangle$. The other planar hexagon pulses will have larger Bravais–Miller indices, and we expect heuristically that these interfaces have higher energy. These pulses can be computed in exactly the same fashion as the $\langle 10\rangle$ and $\langle 11\rangle$ pulses, but we have not carried out these computations at present. The existence of infinitely many planar hexagon pulses with different orientation can also be inferred from an energy argument. At the Maxwell point, a single hexagon cell has zero energy and so any combination of the hexagon cells that lie on the hexagon lattice can be used to create differently orientated pulses. We expect the resulting pulses to pin or lock to produce snaking regions similar to those found for $\langle 10\rangle$ and $\langle 11\rangle$ pulses.

Finally, we briefly address the nature of the pitchfork bifurcations to almost-planar hexagon pulses that occur near each fold bifurcation. We begin with the fold bifurcation: the eigenfunction $v_0(x, y)$ associated with the fold eigenvalue $\lambda = 0$ is periodic in the y-variable with minimal period $\ell = 4\pi/\sqrt{3}$ for $\langle 10\rangle$ and

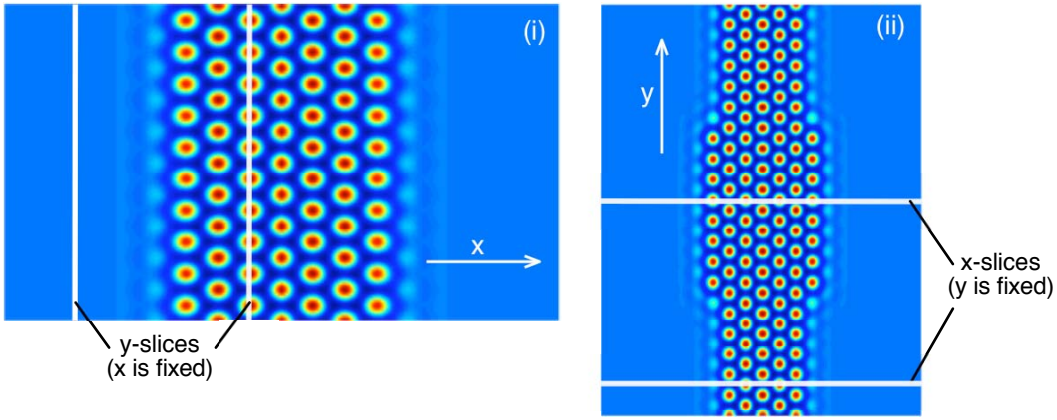

Figure 17: *Panel (i) contains a color plot of a planar* $\langle 10 \rangle$ *hexagon pulse. We view* x *as the evolution variable which is used to evolve* y*-slices forward and backward: the left* y*-slice corresponds to an equilibrium of the resulting spatial dynamical system in* x *(the profile in the* y*-slice does not change when* x *is varied nearby), while the* y*-slice in the hexagon region corresponds to a periodic orbit (the profile changes periodically in* x *when the* y*-slice is moved to the left and right). Thus, we can interpret a planar* $\langle 10 \rangle$ *hexagon pulse as a homoclinic orbit that passes close to a periodic orbit which is formed of hexagons, and we therefore expect snaking on account of the results in §2.1 and §3.2. Panel (ii) contains a color plot of an almost-planar hexagon pulse. Here, we view* y *as the evolution variable which propagates* x*-slices up- and downwards. The two indicated* x*-slices correspond to two different periodic orbits: their profiles change periodically when* y *is varied, but the horizontal extent of the hexagon regions is different for the two profiles. We can therefore interpret an almost-planar hexagon pulse as a homoclinic orbit in the* y*-dynamics which connects the periodic orbit at top and bottom to itself and which passes near a second periodic orbit. The results in §2.1 and §3.2 imply again that snaking should occur.*

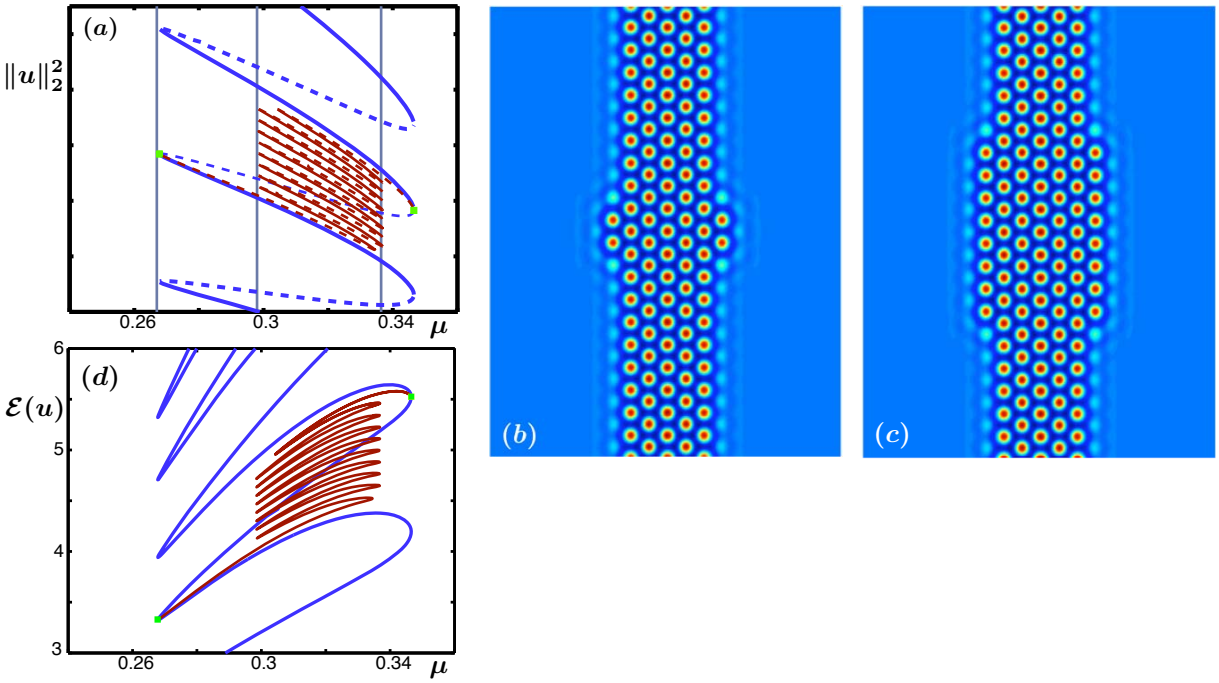

Figure 18: *In panel (a), the bifurcation diagrams of planar* $\langle 10 \rangle$ *hexagon pulses [blue] and the bifurcating almost-planar pulses [red] are shown, where stable pulses are indicated by solid lines and unstable ones by dashed lines. Panels (b)-(c) are color plots of two different almost-planar hexagon pulses for* $\mu = 0.3$ *along the smaller red snaking diagram. In panel (d), we plot the energy* $\mathcal{E}(u)$*, computed as an integral over the entire computational domain, along the branches.*

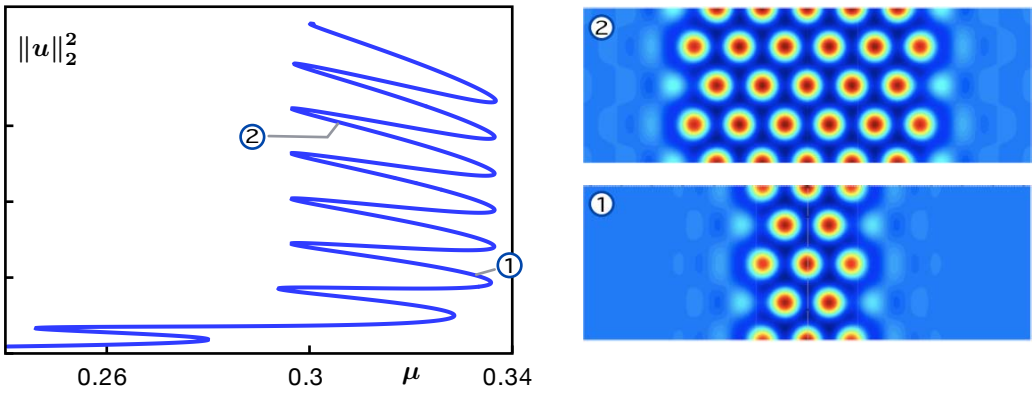

Figure 19: *The left panel contains the bifurcation diagram of planar* $\langle 11 \rangle$ *hexagon pulses. Two selected profiles are shown on the right.*

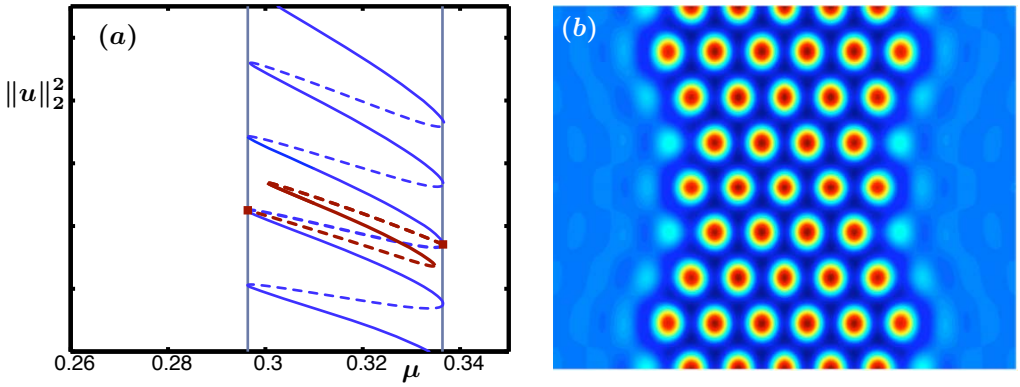

Figure 20: *The bifurcation diagrams of planar* $\langle 11 \rangle$ *hexagon pulses [blue] and the bifurcating almost-planar pulses [red] are plotted in panel (a). Panel (b) is a color plot of an almost planar* $\langle 11 \rangle$ *pulse for* $\mu = 0.309$.

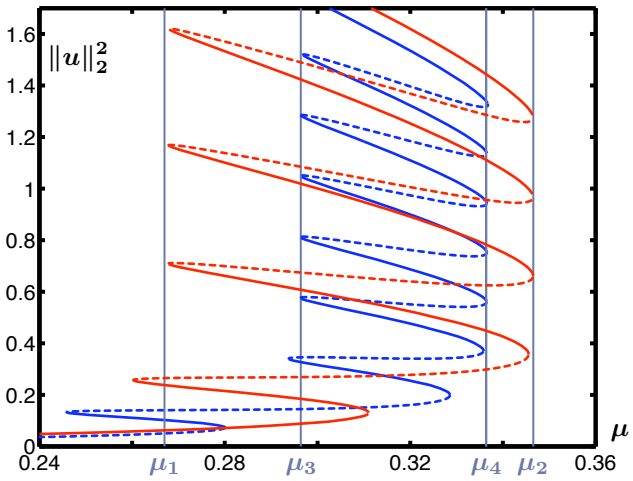

Figure 21: *The bifurcation diagrams of planar hexagon pulses with Bravais–Miller indices* $\langle 10 \rangle$ *(in red) and* $\langle 11 \rangle$ *(in blue) are shown. The* $\langle 10 \rangle$ *pulse snakes between the limits* $\mu_1 = 0.267$ *and* $\mu_2 = 0.3454$*, while the* $\langle 11 \rangle$ *pulse snakes between* $\mu_3 = 0.2964$ *and* $\mu_4 = 0.3364$*. The stability of the branches alternates between unstable [dashed] and stable [solid] at each fold.*

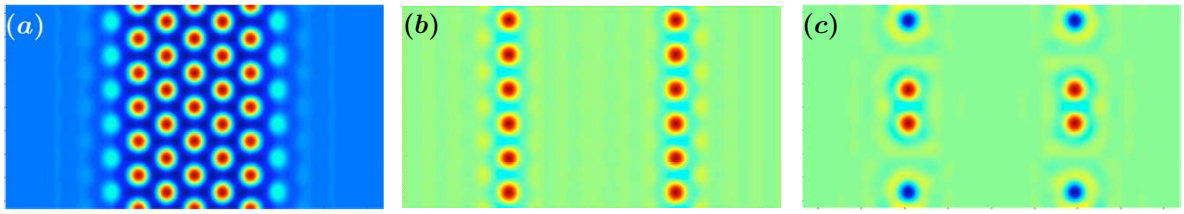

Figure 22: *Shown are color plots of a planar* $\langle 10 \rangle$ *hexagon pulse at a fold bifurcation in (a), the associated fold eigenfunction in (b), and the pitchfork eigenmode that leads to almost-planar hexagon pulses in (c).*

$\ell = 4\pi$ for $\langle 11 \rangle$ pulses. Now consider the planar pulse on the entire plane and apply Floquet–Bloch theory, see for instance [67, Theorem 2.1]: we find a one-parameter family $\lambda(\gamma)$ of eigenvalues, defined for all γ sufficiently close to zero, whose eigenfunctions are of the form $v(x, y; \gamma)\mathrm{e}^{\mathrm{i}\gamma y}$, where $v(x, y; \gamma)$ has period ℓ in the y-variable. For $\gamma = 0$, we recover the fold eigenvalue $\lambda(0) = 0$ with eigenfunction $v(x, y; 0) = v_0(x, y)$. Next, we consider domains of height $N\ell$ in the y-direction for large integers $N \gg 1$ with periodic boundary conditions in y: this is the situation shown in Figure 16. The eigenfunctions we found on the plane fit into this domain provided $\gamma = \gamma_n := 2\pi n/N\ell$ for integers $n \geq 0$. The smallest nonzero value of γ is $\gamma_1 = 2\pi/N\ell$: the associated eigenvalue $\lambda(\gamma_1) = \mathrm{O}(1/N)$ is close to zero for $N \gg 1$, and its eigenfunction

$$v(x, y; \gamma_1)\mathrm{e}^{\mathrm{i}\gamma_1 y} = [v_0(x, y) + \mathrm{O}(1/N)]\mathrm{e}^{2\pi \mathrm{i} y/N\ell}$$

is a harmonic modulation of the fold eigenfunction in the y-direction. Figure 22 shows a $\langle 10 \rangle$ hexagon pulse and the associated fold and pitchfork eigenfunctions on a domain with $N = 6$: the pitchfork eigenfunction is indeed a cosine modulation of the fold eigenfunction with maximal period in y as claimed.

5.3 Localized hexagon patches

In this section, we discuss our results for localized hexagon patches of the planar Swift–Hohenberg equation (1.1). We shall also report on numerical results for localized radial pulses[7]. We focus first on two different representative slices $\nu = 0.9$ and $\nu = 1.6$ of the bifurcation diagram in (μ, ν)-parameter space, before we consider the full diagram in (μ, ν)-space and comment on the special value $\nu = 1.049$ that separates regions of qualitatively similar behavior.

5.3.1 Bifurcation diagram for $0 < \nu < 1.049$

We first consider the region where $0 < \nu < 1.049$ and illustrate our results in Figure 23 for $\nu = 0.9$. We find localized radial pulses, localized hexagon patches, and regular hexagons. All these solutions bifurcate from $u = 0$ at $\mu = 0$ and are initially unstable. Regular hexagons stabilize in a fold bifurcation and later cross into the left half-plane $\mu < 0$. Localized radial pulses gain stability with respect to radial perturbations at the first fold bifurcation but continue to be unstable with respect to hexagonal perturbations. They cross with nonzero amplitude into the left half-plane, where they turn into non-localized target patterns. The unstable localized hexagon patches appear to begin to snake for $\mu \approx 0.065$, but we were only able to continue through the first fold. The Maxwell point of regular hexagons for $\nu = 0.9$ is $\mu = \mu_{\mathrm{M}} \approx 0.07$.

5.3.2 Bifurcation diagram for $1.049 < \nu < 2.23$

In Figure 24, we summarize the bifurcation diagram for $\nu = 1.6$, where localized hexagon patches have previously been found in [78] via direct numerical simulations. The localized hexagon patches that arise in this parameter region tend to be highly localized, and the numerical methods described in §4 should therefore work particularly well. Other previous direct numerical simulations have shown that temporally

[7] Existence results for these localized radial solutions are proved in [58]

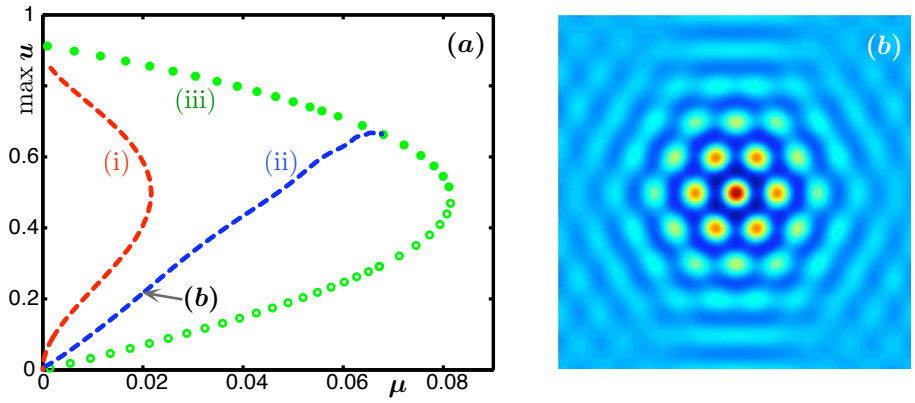

Figure 23: *Localized radial pulses (i), localized hexagon patches (ii), and regular hexagons (iii) with wavenumber* $\kappa = 1$ *of the planar Swift–Hohenberg equation (1.1) with* $\nu = 0.9$ *are shown in panel (a). Dashed solutions and regular hexagons with open bullets are unstable, while regular hexagons with filled bullets are stable. Note that neither branch (i) nor (ii) terminates at the branch (iii) of regular hexagons [see text for details]. Panel (b) contains a color plot of a localized hexagon patch for* $\mu = 0.02$.

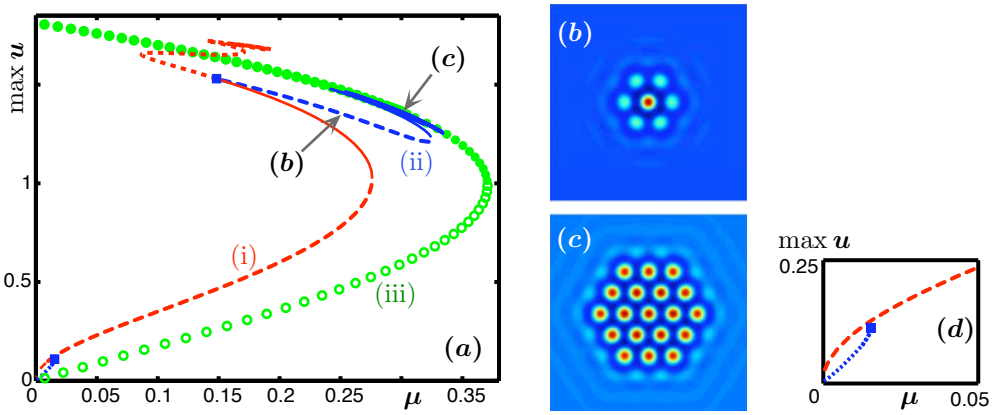

Figure 24: *Localized radial pulses (i), localized hexagon patches (ii), and regular hexagons (iii) with wavenumber* $\kappa = 1$ *of the planar Swift–Hohenberg equation (1.1) with* $\nu = 1.6$ *are shown in panel (a); the area near the origin is enlarged in panel (d). Dashed solutions and regular hexagons with open bullets are unstable, while solutions along solid lines and regular hexagons with filled bullets are stable. Panels (b) and (c) are color plots of localized hexagon patches for* $\mu = 0.25$ *near the bifurcation off the radial pulse (b) and for* $\mu = 0.3$ *on the snaking curve (c).*

stable localized radial pulses exist in this region of parameter space: our numerical continuation methods will corroborate these findings and establish a strong link between localized radial and hexagonal structures.

As shown in Figure 24, radial pulses bifurcate off the trivial solution at $\mu = 0$ and are initially unstable with respect to radial and hexagonal perturbations. Also bifurcating at $\mu = 0$ are unstable localized hexagon patches which disappear in a subcritical pitchfork bifurcation of the radial pulse at $\mu \approx 0.015$: from this point onward, the radial pulses are unstable only with respect to radial perturbations. Subsequently, the radial pulses stabilize in a saddle-node bifurcation at $\mu \approx 0.276$ and later on, for $\mu \approx 0.15$, undergo a second subcritical bifurcation to unstable localized hexagon patches. The radial pulses continue on and begin to snake. The unstable localized hexagon patches that bifurcate at the second pitchfork bifurcation of the radial pulses gain stability in a fold bifurcation at $\mu \approx 0.325$ and begin to snake around the hexagon Maxwell point $\mu_{\rm M} \approx 0.3222$. While snaking, the localized hexagon patches become wider until they fill the entire domain. In addition to these localized patterns, unstable regular hexagons also bifurcate from the trivial solution at $\mu = 0$ and stabilize in a fold bifurcation at $\mu \approx 0.37$. As can be seen from Figure 24(a), the localized hexagon patterns snake close to the regular hexagons.

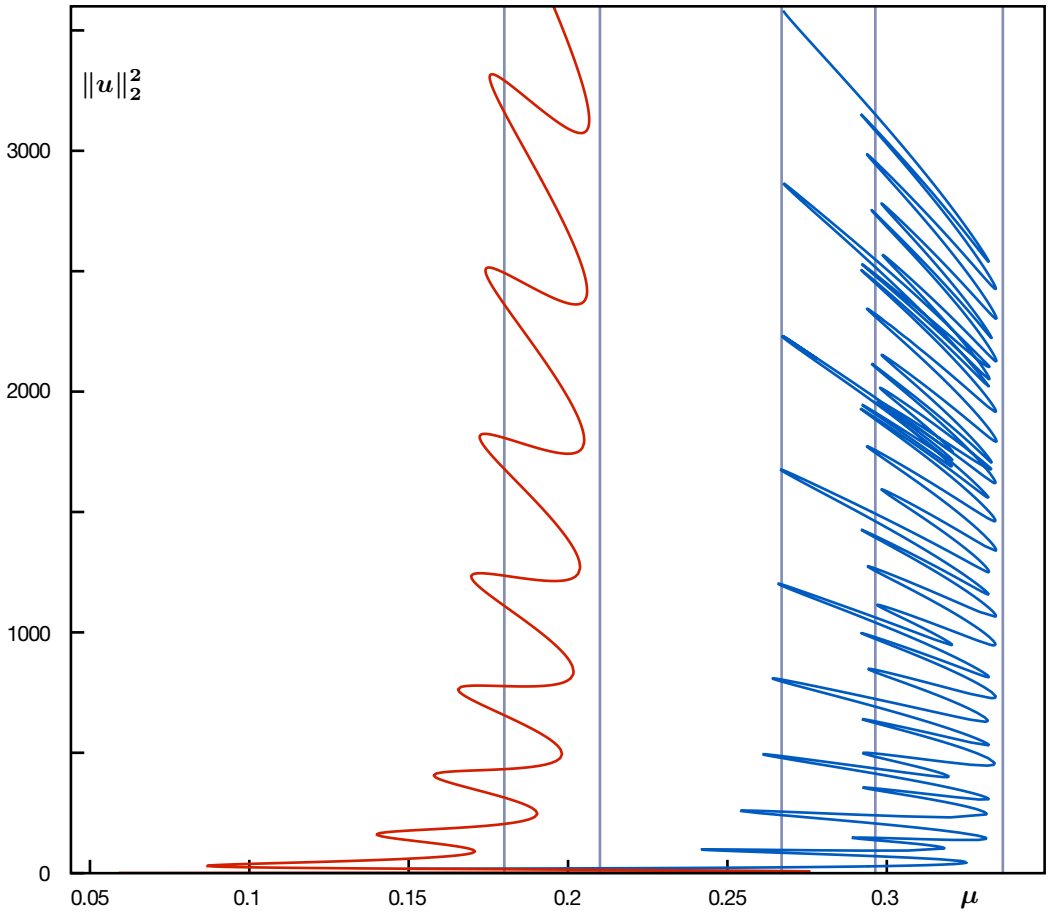

Figure 25: *The snaking curves of radial pulses [left in red] and fully localized hexagon patches [right in blue] are plotted for $\nu = 1.6$. Radial solutions are computed on a disk of radius $R = 100$: the fold asymptotes of 1D rolls are indicated by vertical grey lines, and the Maxwell point of 1D rolls occurs at $\mu_{\rm M} = 0.2$. The localized hexagon patches are computed with $M = 19$ angular Fourier modes on a domain of radius $R = 80$: the fold asymptotes of planar $\langle 10\rangle$ and $\langle 11\rangle$ hexagon pulses are plotted as vertical grey lines, and the hexagon Maxwell point occurs for $\mu_{\rm M} \approx 0.3222$. The hexagon snaking curve and the associated solution profiles can be viewed in this [MOVIE].*

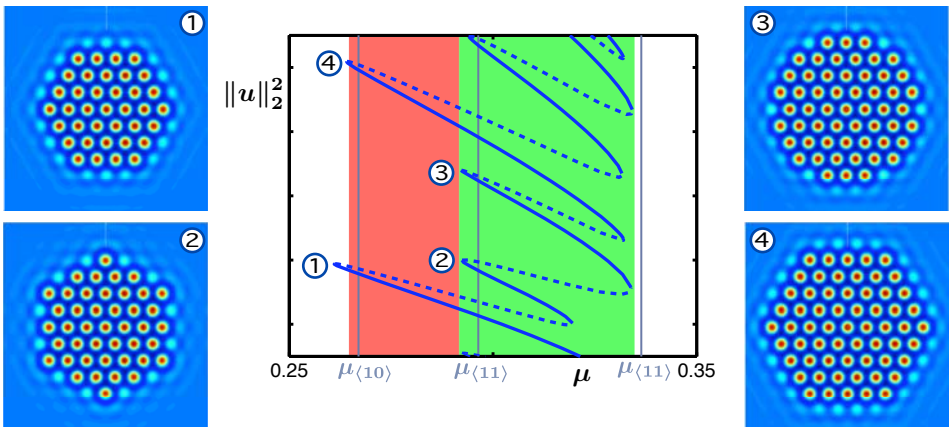

Figure 26: *The center panel contains part of the bifurcation diagram of localized hexagon patches for $\nu = 1.6$. Stable and unstable solutions are plotted in solid and dashed lines, respectively. The vertical lines in grey correspond to the fold limits of planar $\langle 10\rangle$ and $\langle 11\rangle$ hexagon pulses. The red and green regions indicate where temporal self-completion, as shown in Figure 31(b) and (c), does or does not occur, respectively. Panels 1-4 contain color plots of the hexagon patches at the inner and outer left folds.*

We focus now on the snaking behavior of localized hexagon patches. The bifurcation curves of localized radial and hexagon patterns are shown in Figure 25. In particular, we see that the snaking of localized hexagon patches is qualitatively very different from the snaking of the radial pulses and, in fact, also from the snaking of planar hexagon fronts whose diagram is shown in Figure 21. Indeed, the fold bifurcations of radial pulses and planar hexagon pulses occur near two well-defined limiting values, while the folds of localized hexagon patches align themselves along at least three distinct vertical asymptotes.

The spatial shapes of the fully localized hexagon patches along the snaking curve can be viewed in the accompanying movie. It is clear from the movie that the localized hexagon structures change in a complicated fashion as the parameter μ is varied, and we shall now discuss some of the features visible in the movie in more detail and attempt to identify the underlying mechanisms.

In Figure 26, we plot a few selected spatial profiles along a small segment of the bifurcation curve. We note that localized structures alternately lose and regain stability at consecutive folds. Moving along the bifurcation branch from panel (1) to panel (4) in Figure 26, we see that the localized structure acquired an additional ring of hexagons and thus grew from four to five rings. The process of adding rings is much more complicated than simply adding a new full ring at each fold. First, as shown in panel (2), a single hexagon is added at the center of each side: note that the faces of the resulting localized structure resemble the planar $\langle 11 \rangle$ hexagon pulses encountered in §5.2 and that the addition of the single hexagon occurs at a fold that aligns itself with the snaking curve of $\langle 11 \rangle$ pulses. Next, in panel (3), hexagons are added symmetrically to either side of the centered hexagon cell created previously in panel (2): this happens again near an inner fold. The final step is to add an additional pair of hexagons symmetrically to either side of the previously created hexagons to complete the row: this occurs near the fold corresponding to a $\langle 10 \rangle$ pulse. The faces of the "super-hexagon" structure in panels (1) and (4) resemble planar hexagon pulses with $\langle 10 \rangle$ orientation. In summary, as the snake in Figure 26 is traversed, new hexagon cells emerge symmetrically on each face, starting at the center of each face. This cellular growth is reminiscent of the bifurcation diagram of almost-planar $\langle 10 \rangle$ pulses shown in Figure 18.

Figure 27 contains a sequence of pictures of localized hexagon structures further up on the snaking curve to illustrate the transition from a localized structure with nine hexagon rings to a pattern with ten rings. Comparing panels (1) and (2), we find that two new hexagon cells appear in the center of each face: there are two new hexagon cells, rather than just one, as the number of hexagons in the outer-most row in Figure 27(1) is odd, rather than even as for the 4-ring structure in Figure 26. While cells are added in the center, the corners of the super-hexagon structure recede and disappear, which did not happen for 4-ring structures. In panel (3), the diagonal faces resemble planar $\langle 11 \rangle$ pulses which move forward to complete the super-hexagon visible in panel (7) as we move along the bifurcation curve. The removal of the six cells in the corners of the super-hexagon in panels (1)-(2) leads to a reduction of the L^2-norm of the localized structures which creates the apparent self-intersections of the bifurcation curve visible in Figure 25.

The results discussed above indicate that localized hexagon patches expand initially by adding one or two new hexagon cells at the center of each face. In Figure 28, we compare the bifurcation curves of almost-planar $\langle 10 \rangle$ hexagon pulses with one and two cells to the relevant segments of the snaking curve of localized hexagon patches. The parameter values for the first two folds along the bifurcation curves agree well, but the bifurcation curves of almost-planar pulses and localized hexagon patches separate soon after. On a heuristic level, we believe that hexagon patches do not grow by adding full rows because it costs too much energy to grow hexagons at the corners where two adjacent faces join up. This belief is supported by the observation that the corner hexagons actually recede as visible in panels (1)-(2) of Figure 27. Thus, even though cells initially emerge at the centers of each face, the overall growth mechanism is clearly more global, which is why the bifurcation curves of the almost-planar $\langle 10 \rangle$ hexagon pulses agree with the snaking curve of hexagon patches only initially.

We believe that infinitely many planar hexagon fronts with different Bravais–Miller indices play a role in forming the bifurcation diagram shown in Figure 25 though we were not able to go up far enough on the bifurcation curve to identify additional vertical asymptotes that may belong to planar hexagons with different

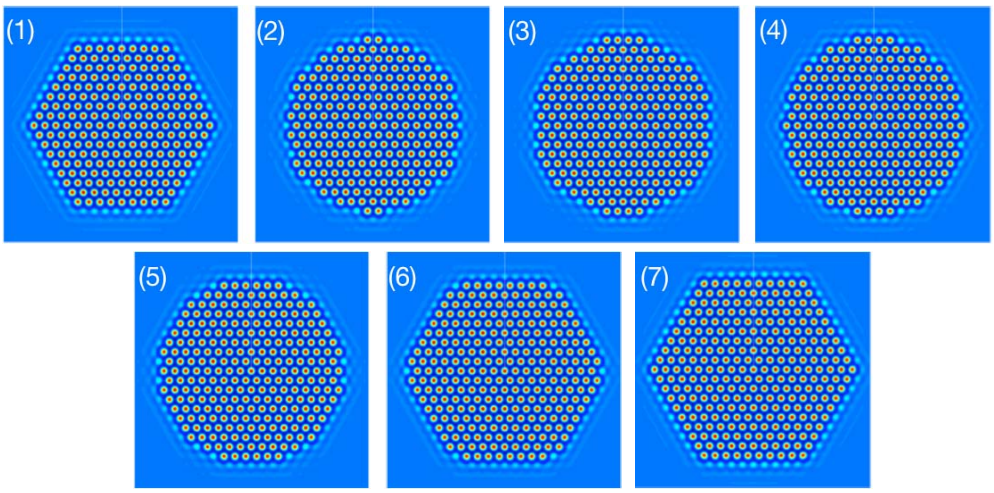

Figure 27: *Color plots of localized hexagon patches at the left-most folds are shown to illustrate the growth from a 9-ring hexagon patch to a 10-ring patch. The computations are done on a domain of radius* $R = 100$ *with* $M = 40$ *angular Fourier modes.*

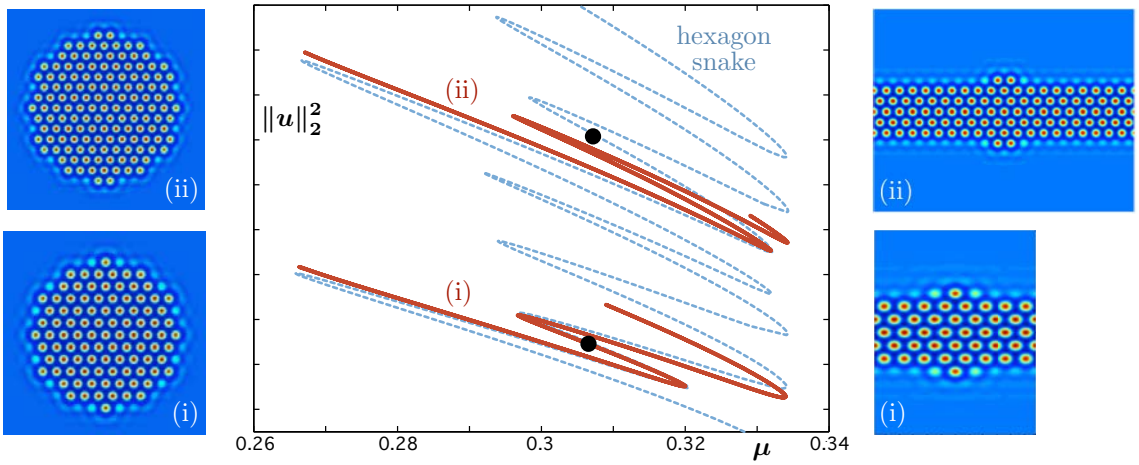

Figure 28: *In the middle panel, we plot part of the hexagon snake from Figure 25 and overlay the snaking curves of almost planar* $\langle 10 \rangle$ *hexagon pulses for which initially one cell (i) or two cells (ii) emerge at the center. We rescaled the vertical coordinate of the snaking curves of the almost planar pulses linearly to allow a comparison with the hexagon data. The remaining panels show color plots of localized hexagon patches [left] for parameter values indicated by bullets in the middle panel and representative almost-planar pulses [right] on the curves (i) and (ii).*

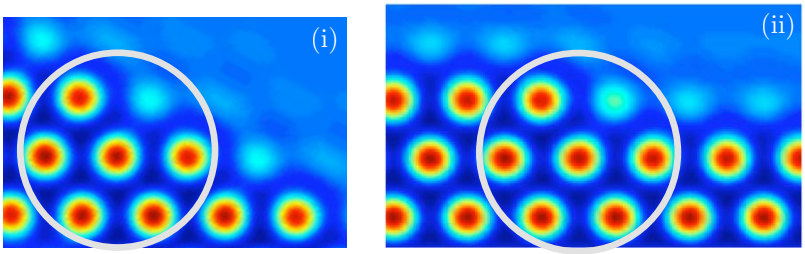

Figure 29: *We plot a rotated planar* $\langle 11 \rangle$ *hexagon pulse in panel (i) and an almost planar* $\langle 10 \rangle$ *hexagon pulse in panel (ii). The circles enclose incomplete hexagon structures: along the next fold in the snaking curve, the missing hexagon in the circle will be filled in.*

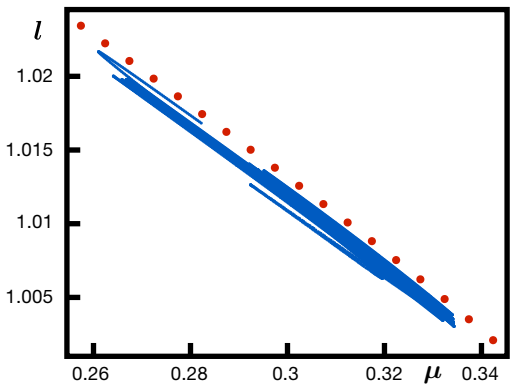

Figure 30: *Plotted are the wavelengths $l = 1/\kappa$ of the regular hexagons for which $\mathcal{H} = 0$ [red bullets] and of the hexagon cells located at the center of the localized hexagon patches [blue dots] as functions of μ for $\nu = 1.6$. The wavelength $l = 1$ corresponds to a spatial period of 2π.*

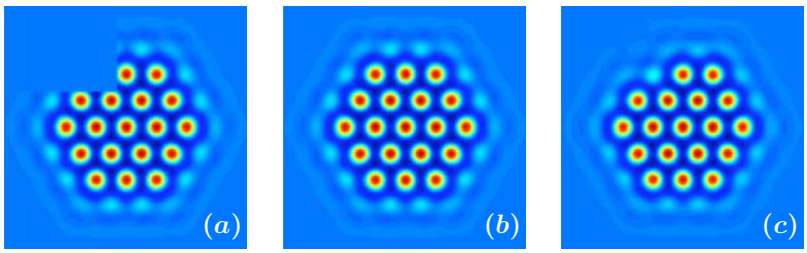

Figure 31: *We illustrate the temporal evolution of localized hexagon structures in the Swift–Hohenberg equation (1.1) with $\nu = 1.6$. The initial condition is shown in panel (a). The solutions at time $t = 100$ are shown in panel (b) for $\mu = 0.27$ inside the red region of Figure 26 and in panel (c) for $\mu = 0.3$ inside the green region of Figure 26.*

indices. It is remarkable though that all rightmost folds seem to line up near the asymptote coming from the planar $\langle 11 \rangle$ hexagon pulse. Most of these folds seem to involve structures that resemble either planar $\langle 11 \rangle$ or almost-planar $\langle 10 \rangle$ pulses. On a heuristic level, it appears that growing these structures involves the same mechanism, and we illustrate this further in Figure 29. However, hexagons emerge along the entire interface of a planar $\langle 11 \rangle$ pulse, while only a single hexagon is added to an almost-planar $\langle 10 \rangle$ structure.

In §3.2, we showed that regular hexagon cells in a stationary planar hexagon front satisfy $\mathcal{H} = 0$ for the conserved quantity $\mathcal{H}$ that we defined in (3.8). The condition $\mathcal{H} = 0$ selects the wavenumber of these hexagons. In §3.2, we stated our belief that this selection criterion for the wavenumber should also apply to localized hexagon patches. In Figure 30, we compare the wavenumbers of regular hexagons for which $\mathcal{H} = 0$ with the wavenumbers of the hexagon cells at the center of localized hexagon patches. We find that the wavenumbers of the center hexagon cells in localized hexagon patches get closer to the predicted wavenumbers as we move up on the snaking curve.

The different vertical asymptotes visible in Figure 26 have interesting consequences for the temporal dynamics of the Swift–Hohenberg equation. As indicated in Figure 26, we divide the μ-parameter space into two intervals, shown in red and green, depending on whether we are to the left or right of the folds that are aligned with the left-most asymptote of the planar $\langle 11 \rangle$ hexagon pulse. These regions seem to be intimately linked with different self-completion behaviors of localized hexagon patches. We choose the pattern shown in Figure 31(a) as our initial condition and solve the planar Swift–Hohenberg equation. For μ in the red region, to the left of the left-most $\langle 11 \rangle$ fold, the solution evolves in time towards the completed super-hexagon shown in Figure 31(b): since $\langle 11 \rangle$ pulses do not exist in this parameter region, the pattern evolves in time so that all interfaces are $\langle 10 \rangle$ pulses. In contrast, for μ in the green region to the right of the left-most $\langle 11 \rangle$ fold, the solution converges in time to a localized hexagon patch that is not $\mathbb{D}_6$-symmetric: stable $\langle 11 \rangle$ pulses exist in

this region, and the interface of the pattern finds it easier to evolve towards a $\langle 11 \rangle$ pulse rather than a $\langle 10 \rangle$ pulse. Phrased in terms of the bifurcation diagram of Figure 26, the solution moves upward to the stable $\mathbb{D}_6$-symmetric pattern on the hexagon bifurcation curve for parameters in the red region. In contrast, the solution evolves to an asymmetric hexagon patch for parameters in the green region: it appears as if the asymmetric patterns block the evolution towards symmetric patches. We conjecture that these asymmetric hexagon patches may bifurcate from $\mathbb{D}_6$-symmetric hexagon patches in a planar version of ladders, similar to those observed in one space dimension in [19, 20, 22] which we reproduced in Figure 8.

5.3.3 Bifurcation diagram in (μ, ν)-parameter space

Using numerical continuation, we have also traced out partial bifurcation diagrams for localized patterns of the planar Swift–Hohenberg equation in the parameters (μ, ν). These results are summarized in Figure 33 and presented in schematic form in Figure 32.

Regular hexagons exist above the green curve in Figure 33(a). We find that localized hexagon patches seem to bifurcate from the trivial state $u = 0$ along the entire positive ν-axis into the positive quadrant $\mu > 0$. Hexagon patches also bifurcate from localized radial spots along a pitchfork bifurcation curve, where symmetry is broken from O(2) to $\mathbb{D}_6$. Overall, we obtain a connected surface along which localized hexagon patches exist: see Figure 32 for a schematic picture and Figures 23 and 24 for numerical computations. Localized spots are stable in a wedge delimited by the fold and pitchfork bifurcation curves that emerge from the mode interaction point $(\mu, \nu) = (0.048, 1.049)$ $(\nu^2 = 1.1)$ in Figure 33(a).

Localized hexagon patches snake in a wedge-like region which is aligned with the hexagon Maxwell curve and appears to extend all the way to the origin, where the bifurcation to regular hexagons changes from super- to subcritical, as outlined in Figure 32(b). In Figure 33(c), we show four numerically continued fold bifurcation curves of localized hexagon patches which disappear in two cusp bifurcations. For $\nu \leq 0.9$, localized hexagon patches are spread out so far and fold bifurcations occur so close to each other that we were not able to continue beyond the first fold: these numerical difficulties prevented us from further probing the sequence of fold and cusp bifurcations. Spots also snake, and we show in Figure 33(a) the region delimited by the first two fold bifurcation curves along their snaking curve together with the cusp at which the fold curves collide and disappear. Again, we expect that the snaking region of spots extends along the Maxwell curve associated with 1D rolls to the codimension-two point $(\mu, \nu) = (0, \sqrt{27/38})$ where the bifurcations to rolls changes from super- to subcritical.

In Figure 26, we observed that the left-most snaking limit of the hexagon patches coincides with the left-most fold of the planar $\langle 10 \rangle$ hexagon pulses. To illuminate this feature further, we show in Figure 34 the snaking region of fully localized hexagon patches and, for comparison, the snaking regions of planar $\langle 10 \rangle$ and $\langle 11 \rangle$ hexagon pulses in panels (a) and (b), respectively. For $\mu < 0.35$, the left-most fold curve of the $\langle 10 \rangle$ pulses aligns itself with the left-most boundary of the hexagon patches, while the right-most fold curve of the $\langle 11 \rangle$ pulses aligns itself with the right-most boundary of the hexagon patches.

We see in Figure 33 that a cusp forms at $(\mu, \nu^2) \approx (0.4205, 5.4173)$ on the upper fold curve on the wedge belonging to localized hexagon patches. This upper cusp is similar to that found in [19, 20, 22] for 1D structures and indicates that a new Maxwell curve crosses into the snaking region. We plot a localized hexagon patch further up on the upper fold curve for $(\mu, \nu^2) = (0.7, 6.2355)$ in Figure 35(a): note that the individual hexagon cells on the outer ring are elongated. For comparison, we plot in Figure 35(b) the localized hexagon patch at the lower cusp at $(\mu, \nu^2) = (0.0738, 0.8612)$.

5.4 Localized rhomboid patches

We also investigated fully localized rhomboid patches. These solutions have an interior cellular hexagonal structure but, as shown in Figure 36(b), the overall patch does not possess hexagonal symmetry: the underlying cellular pattern is shifted by half a spatial period so that the center of the localized patch does

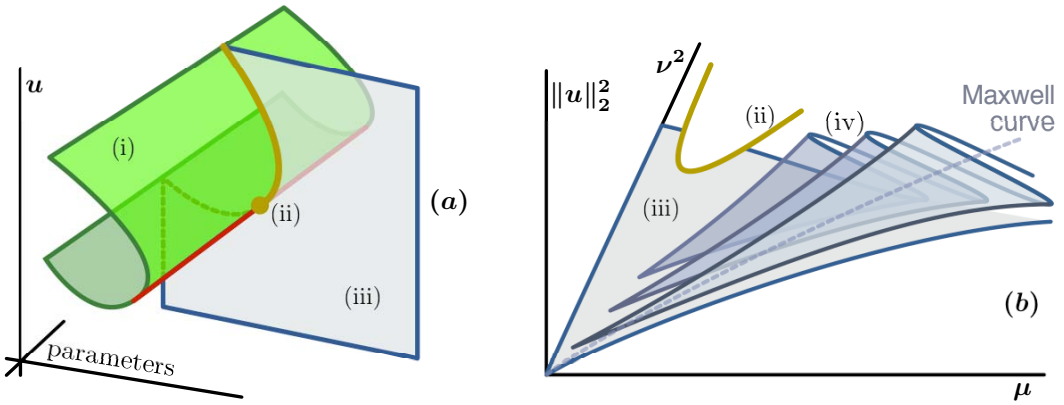

Figure 32: *Schematic illustrations of the bifurcation diagram of localized hexagon patches are shown. Panel (a) shows the sheet of localized radial spots (i) which undergo pitchfork bifurcations to localized hexagon patches along the yellow curve (ii). In panel (b), localized hexagon patches (iii) bifurcate from $u = 0$ at $\mu = 0$ and from spots along the pitchfork bifurcation curve (ii). The hexagon patches begin to snake (iv) near the hexagonal Maxwell curve (shown in dotted grey) in an infinite sequence of fold bifurcations that disappear closer to the origin in a sequence of cusps. See Figure 33(c) for the corresponding numerical results.*

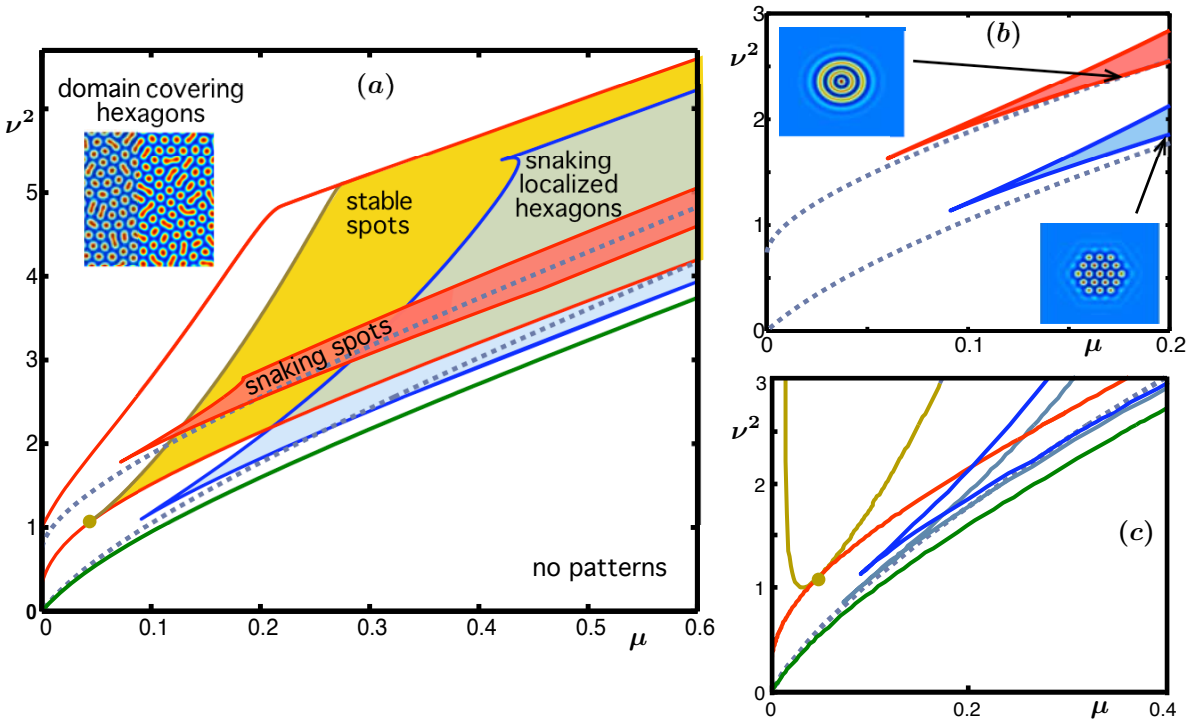

Figure 33: *This figure summarizes our numerical results for radial and hexagonal patterns in the planar Swift–Hohenberg equation (1.1). Dashed grey curves correspond to 1D roll and 2D hexagonal Maxwell curves, the green curve corresponds to the disappearance of regular hexagons with wavenumber $\kappa = 1$ in a fold bifurcation, and red curves correspond to fold bifurcations of localized radial spots. The existence region of stable spots is shown in yellow in panel (a). Panels (a)-(c) also indicate the snaking regions of spots and localized hexagon patches that are delimited by the first pair of fold bifurcations of these patterns: as discussed in the main text, we expect that there is a sequence of fold curves which disappear in a sequence of cusps that accumulate at the origin, so that the full snaking regions are expected to extend along the two Maxwell curves all the way to the ν-axis. Panel (c) contains four such fold bifurcation curves of localized hexagon patches that are aligned along the hexagon Maxwell curve and which disappear at two cusp bifurcations. Panel (c) also contains the pitchfork bifurcation curves of localized hexagon patches from spots in yellow and the fold bifurcation curve of spots in red: these curves meet at the mode interaction point $(\mu, \nu^2) = (0.048, 1.1)$ $(\nu = 1.049)$.*

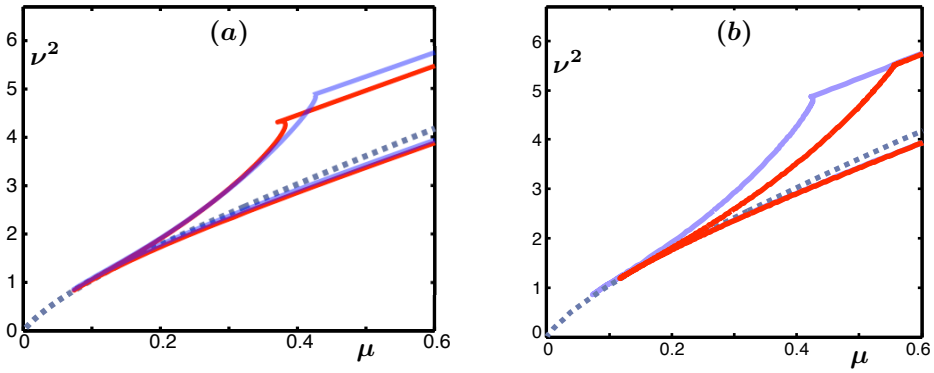

Figure 34: *Comparison of the snaking region of localized hexagon patches [blue] and the snaking regions of planar* $\langle 10 \rangle$ *hexagon pulses [red] in panel (a) and* $\langle 11 \rangle$ *hexagon pulses [red] in panel (b). The hexagon Maxwell curve is also shown [dashed grey].*

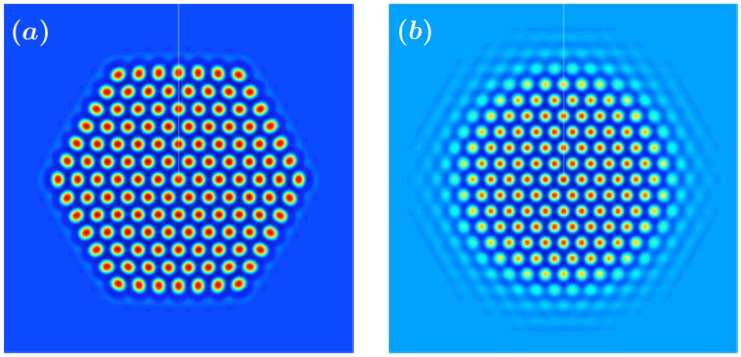

Figure 35: *Panels (a) and (b) contain color plots of localized hexagon patches for* $(\mu, \nu^2) = (0.7, 6.2355)$ *and* $(\mu, \nu^2) = (0.0738, 0.8612)$*, respectively.*

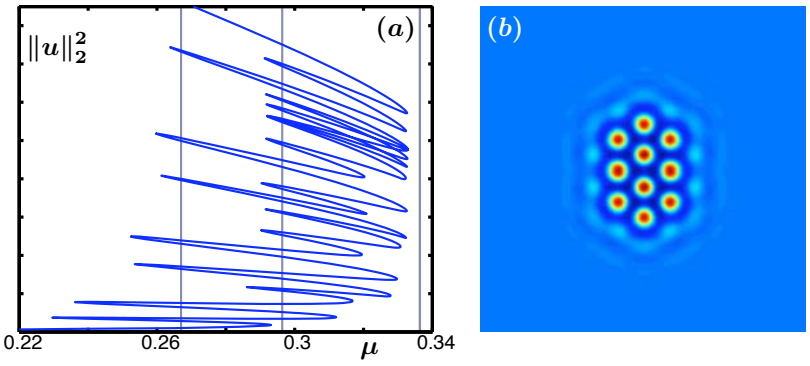

Figure 36: *Panel (a) contains the bifurcation diagram of localized rhomboid patches for* $\nu = 1.6$*, while the rhomboidal structure itself is shown as a color plot in panel (b) for* $\mu = 0.2817$*. The vertical lines are the asymptotes of the fold bifurcations of* $\langle 10 \rangle$ *and* $\langle 11 \rangle$ *hexagon pulses shown in Figure 26. The computations were carried out on a square domain with dimensions* 80×80*.*

not coincide with the center of an interior hexagon. Unlike localized hexagon patches, localized rhomboids bifurcate from a pair of localized hexagons, which in turn bifurcate from the trivial state. Hexagon pairs, triplets, and rhomboids consisting of four hexagons have previously been computed in [63]. The snaking diagram of the localized rhomboid patches, shown in Figure 36(a), appears to be qualitatively similar to the snaking diagram of localized hexagon patches shown in Figure 25. There seem to be roughly three snaking limits: the left-most limit corresponds to the completion of a super-rhomboid, shown in Figure 36(b), while the other two snaking limits correspond to the emergence of individual hexagons along the sides of the localized structure as in the case of hexagon patches. Further up the snake, the left-most folds get closer to the folds of the planar $\langle 10 \rangle$ hexagon pulses. Similar to the case of hexagon patches, the bifurcation curves of localized rhomboids intersect as individual corner cells are suppressed, leading to a decrease of the overall L^2-norm. We computed the localized rhomboids on a large square box with Neumann boundary conditions rather than with polar coordinates as we did for localized hexagon patches: in particular, we are confident that the damping of the corner cells is not due to boundary conditions or numerical errors.

We believe that the localized hexagon and rhomboid patches are connected in parameter space by bifurcation curves of asymmetric patterns similar to those found in [19, 21] for 1D structures. These ladders will effectively shift the cellular pattern between the localized hexagon and rhomboid patches.

6 Conclusions and discussion

Summary. We briefly summarize our main findings. First, we provided a selection principle for hexagons that can appear as asymptotic states in planar fronts that connect to the trivial state $u = 0$. Any such hexagon must satisfy $\mathcal{H} = 0$ where the function $\mathcal{H}$ is a first integral of the spatial dynamical system that describes solutions $u(x, y)$ of the Swift–Hohenberg equation that are periodic in the transverse y-direction. The expression (1.6) of $\mathcal{H}$ was derived from a conservation law that arises, via Noether's theorem, due to the translation symmetry of the Lagrangian of the energy (1.4) of the Swift–Hohenberg equation. Using a theorem proved in [9], we also showed that a unique branch of regular hexagons along which $\mathcal{H} = 0$ bifurcates from the trivial state at $\mu = 0$: these hexagons have a uniquely selected wavelength.

In §3.2, we gave a spatial-dynamics formulation of solutions of the Swift–Hohenberg equation that are periodic in one of the two spatial variables. This formulation implies that planar hexagon pulses, such as those shown in Figures 16 and 19, will exist in open regions of parameter space provided they are transversely constructed, a condition we expect to hold generically. This indicates that snaking should occur for planar hexagon pulses, and we found numerically in §5.2 that snaking does indeed occur for hexagons pulses with two different orientations, namely with Bravais–Miller indices $\langle 10 \rangle$ and $\langle 11 \rangle$. We also computed and continued almost-planar hexagon pulses which bifurcate from the planar hexagon pulses in pitchfork bifurcations near each fold bifurcation: these almost-planar pulses appear prominently in the snaking diagram of localized hexagon patches.

Heuristically, we expect that the snaking regions are centered around the hexagon Maxwell curve which corresponds to the curve in (μ, ν)-parameter space along which hexagons exist that satisfy $\mathcal{H} = 0$ and that have the same energy, $\mathcal{E}(0) = 0$, as the trivial state $u = 0$. Indeed, only when the trivial state and the hexagons have roughly the same energy can we expect that stationary interfaces between them exist; otherwise, one of the states will invade the other one to reduce the overall energy. Our numerical computations confirmed this heuristic picture and showed furthermore that the Maxwell curve emerges from the codimension-two point where the bifurcation to hexagons changes from super- to subcritical, as it is there that we can expect regions of bistability to exist.

Our main numerical findings consist of the continuation results of localized hexagon and rhomboid patches in the Swift–Hohenberg equation. Our computations suggest that infinitely many hexagon and rhomboid patches co-exist in open parameter regions. The localized hexagon patches lie on the same solution branch and increase in width as we move along the branch. Strikingly, the hexagon patches do not grow by adding

a full ring of hexagons at each fold, but instead seem to follow, at least initially, the almost-planar hexagon pulses with indices $\langle 10\rangle$ and $\langle 11\rangle$ that we computed in §5.2. Overall, we found a rich snaking structure with several, possibly infinitely many, vertical asymptotes for fold bifurcations of localized structures, compared with only two asymptotes for planar hexagon pulses and 1D structures. We identified three asymptotes as arising from fold bifurcations of planar hexagon pulses with indices $\langle 10\rangle$ and $\langle 11\rangle$. However, we did not identify an overarching mechanism that predicts how hexagon patches might grow as we move up further along the branch.

We also investigated self-completion of asymmetric hexagon patches and found evidence that self-completion occurs only to the left of the snaking region of the $\langle 11\rangle$ fronts. The self-completion study was motivated by results in [4, 6] where this process was addressed by using interaction theory for localized spots. The alternative explanation put forward here is based on the existence regions of planar hexagon fronts with different orientations. Though we do not have any conclusive evidence, we do not believe that the hexagon structures found in our paper can be viewed as bound states of localized spots: Figure 24, for instance, shows that localized hexagon patches can exist well outside the existence region of localized spots.

Finally, we mention that Figure 33 contains various results on localized radial structures. In particular, the branch of localized hexagon patches that bifurcates from the trivial state at $(\mu, \nu) = 0$ and later begins to snake splits, for larger values of ν, into two branches which begin or end at pitchfork bifurcations of localized radial structures. We refer to [58] for a more detailed analytical and numerical study of these radial spots.

Open problems. We now outline what we believe to be interesting questions for further research on multi-dimensional localized patterns and refer to [50] for another recent list of open problems in this area.

A major goal is to uncover the mechanism that underlies the snaking behavior of localized hexagon patches and to prove that it does occur in the Swift–Hohenberg equation. Currently, there do not seem to be any methods available that can be used to carry out such a comprehensive analysis. Thus, we discuss first a number of more modest open problems that may give better insight into certain aspects of hexagon snaking.

Snaking of planar hexagon pulses seems more amenable to an analytic approach. On a formal level, asymptotics beyond all orders has recently been used in [25, 52] to predict the snaking width for the 1D structures shown in Figure 2 near the codimension-two point $(\mu, \nu) = 0$. The idea behind this approach is to look more closely into the derivation of the amplitude equations (2.10) which govern the existence of 1D pulses. In the standard derivation, anisotropic terms that depend on the small scale x, rather than the large scale $X = \epsilon x$, are neglected. In [25, 52], these terms and their effect on the remaining modes through the nonlinearity are taken into account, and an analysis of the resulting exponentially small coupling terms between rolls and the 1D pulse gave an extremely accurate prediction for the snaking region in the 1D setting. The same approach may perhaps work in the planar case to capture the interaction terms between small-scale hexagons and large-scale hexagon pulses with different Bravais–Miller indices.

The energy functional of the Swift–Hohenberg equation may also help to illuminate snaking of hexagon pulses. Our numerical results indicate that the widths of the snaking regions of planar hexagon pulses depends on the orientation of their interfaces, i.e. on their Bravais–Miller indices, and it may be possible to capture this effect through an appropriate interfacial energy. Along the same lines, the growth of cells along an interface for almost-planar hexagon pulses appears qualitatively similar to the growth of interface boundaries in polycrystalline structures. Numerical studies of polycrystalline structures in [64] via two-dimensional Ising models have shown that the orientation of interfaces in hexagonal lattices has a significant effect on the propagation speed of these interfaces. In the context of the Swift–Hohenberg equation, the speeds of planar $\langle 10\rangle$ and $\langle 11\rangle$ fronts outside the pinning region may be similar to those seen in Ising models.

Another approach to understanding snaking of planar hexagon pulses is to assume that there exists a generic planar hexagon front for a certain value of μ which disappears, as μ decreases or increases beyond a certain threshold, via a saddle-node bifurcation as indicated in Figure 6. Instead of using geometric methods to prove that this results in snaking of planar hexagon pulses, an analytic result via Lin's method could be used

to generalize the intuitive picture given in Figure 6 for two-dimensional Poincaré sections to the infinite-dimensional spatial-dynamics setting of §3.2. This analysis has recently been carried out in [10], where it was also shown that it captures asymmetric ladder structures.

While an analysis of snaking of hexagon patches seems currently out of reach, it may be possible to say more about the underlying mechanisms by carrying out more comprehensive numerical studies. The numerical methods we have used significantly reduce the computational cost required to compute fully localized 2D patterns by using an adaptive mesh and by taking into account the symmetry of localized hexagon patches. However, the computation of larger patterns requires a less expensive way of computing hexagon patches. We believe that implementing triangular finite elements in TRILINOS should result in a significant speed-up. In addition, we do not expect that the core region of hexagon patches changes much as the patterns grow. Thus, it might be possible to work with an annular region as computational domain where the boundary conditions on the inner boundary are chosen to ensure compatibility with previously computed hexagon patches. This should lead to a further reduction of the size of the system.

Other localized 2D patterns. Last, we comment on other localized planar structures.

In [78], fully localized stripe patches were observed in the cubic-quintic Swift–Hohenberg equation

$$u_t = -(1+\Delta)^2 u - \mu u + \nu u^3 - u^5. \tag{6.1}$$

These patterns, reproduced in Figure 1(b), are clearly anisotropic. To describe them, one could use, as in [32], the Newell–Whitehead–Segel equation

$$4\left(\partial_X - \frac{\mathrm{i}}{2}\partial_{YY}^2\right)^2 A = \epsilon A - |A|^2 A + |A|^4 A$$

for the envelope function $A(X,Y)$ of stripes that are parallel to the y-direction, where $(X,Y) = (\epsilon^{1/2}x, \epsilon^{1/4}y)$. This equation admits localized fronts $A_1(X)$ and $A_2(Y)$ with different spatial widths. The front $A_1(X)$ occurs at the 1D Maxwell point found in the normal-form analysis of the one-dimensional cubic-quintic Swift–Hohenberg equation (6.1): this front corresponds to an "equilibrium to periodic orbit" connection for the associated spatial dynamical system, and we therefore expect snaking and the growth of additional rolls along the x-direction as an equation parameter is varied. The front $A_2(Y)$ in the Y-direction, on the other hand, corresponds to an "equilibrium to equilibrium" connection, and we do not expect snaking to occur; instead, we expect that the bifurcation curve converges, in an oscillatory fashion, to a single vertical asymptote [51]. This latter behavior is precisely what was observed in [78] in numerical simulations of fully localized stripe patterns.

Another interesting Swift–Hohenberg model is

$$u_t = -(1+\Delta)^2 u - \mu u + \nu u^3 - u^5 + \alpha \nabla \cdot [|\nabla u|^2 \nabla u].$$

The last term in the above equation gives preference to patterns with square symmetry, and localized patches of squares have indeed been found in direct numerical simulations [44, 79]. We expect that these patches exhibit snaking and predict that localized square patches of square shape grow by adding new cells starting from the middle of each face.

Localized pentagonal structures have also been observed numerically in [91, Figure 10(a)-(b)] in a model of driven optical cavities. Our numerical methods could be extended easily to compute and continue these structures by expanding u as a Fourier series

$$u(r,\theta) = \sum_{n\in\mathbb{Z}} a_n(r) \mathrm{e}^{5n\mathrm{i}\theta}$$

using five-fold symmetric terms. Pentagons do not tile the plane, so the question of snaking for localized pentagons would be interesting.

Acknowledgements. We are grateful to John Burke, Edgar Knobloch, Paul Matthews, Arnd Scheel, and Thomas Wagenknecht for many helpful comments and discussions. We also thank José Antonio Medina Hernández, Gregory Kozyreff, and the anonymous referees for many comments that helped us to improve the presentation of this paper. David Lloyd and Björn Sandstede thank the Newton Institute for the hospitality during the theme programme 'Pattern Formation in Large Domains' in Autumn 2005, and Björn Sandstede gratefully acknowledges a Royal Society Wolfson Research Merit Award.

References

[1] E. Ammelt, Y. A. Astrov, and H.-G. Purwins, *Hexagon structures in a two-dimensional dc-driven gas discharge system*, Phys. Rev. E, 58 (1998), pp. 7109–7117.

[2] S. C. Anco and G. Bluman, *Direct construction method for conservation laws of partial differential equations I: examples of conservation law classifications*, European J. Appl. Math., 13 (2002), pp. 545–566.

[3] ——, *Direct construction method for conservation laws of partial differential equations II: general treatment*, European J. Appl. Math., 13 (2002), pp. 567–585.

[4] I. S. Aranson, K. A. Gorshkov, A. S. Lomov, and M. I. Rabinovich, *Stable particle-like solutions of multidimensional nonlinear fields*, Phys. D, 43 (1990), pp. 435–453.

[5] N. W. Ashcroft and N. D. Mermin, *Solid State Physics*, Harcourt, New York, 1976.

[6] Y. Astrov and Y. Logvin, *Formation of clusters of localized states in a gas discharge system via a self-completion scenario*, Phys. Rev. Lett., 79 (1997), pp. 2983–2986.

[7] D. Avitabile, *Computation of planar patterns and their stability*, PhD thesis, University of Surrey, 2008.

[8] O. Batiste, E. Knobloch, A. Alonso, and I. Mercader, *Spatially localized binary-fluid convection*, J. Fluid Mech., 560 (2006), pp. 149–158.

[9] R. E. Beardmore, M. A. Peletier, C. J. Budd, and M. Ahmer Wadee, *Bifurcations of periodic solutions satisfying the zero-Hamiltonian constraint in reversible differential equations*, SIAM J. Math. Anal., 36 (2005), pp. 1461–1488.

[10] M. Beck, J. Knobloch, D. J. B. Lloyd, B. Sandstede, and T. Wagenknecht, *Snakes, ladders, and isolas of localised patterns*. Preprint, 2008.

[11] C. Bensimon, B. Shraiman, and V. Croquette, *Nonadiabatic effects in convection*, Phys. Rev A, 38 (1988), pp. 5461–5464.

[12] S. Blanchflower, *Magnetohydrodynamic convectons*, Phys. A, 261 (1999), pp. 74–81.

[13] U. Bortolozzo, M. G. Clerc, C. Falcon, S. Residori, and R. Rojas, *Localized states in bistable pattern-forming systems*, Phys. Rev. Lett., 96 (2006), p. 214501.

[14] M. Bougahariou, *Closed orbits of Hamiltonian systems on non-compact prescribed energy surfaces*, Discr. Cont. Dyn. Syst. A, 9 (2003), pp. 603–616.

[15] H. R. Brand, C. Fradin, P. Finn, W. Pesch, and P. Cladis, *Electroconvection in nematic liquid crystals: comparison between experimental results and the hydrodynamic model*, Phys. Lett. A, 235 (1997), pp. 508–514.

[16] C. J. Budd, G. W. Hunt, and R. Kuske, *Asymptotics of cellular buckling close to the Maxwell load*, R. Soc. Lond. Proc. Ser. A, 457 (2001), pp. 2935–2964.

[17] C. J. Budd and R. Kuske, *Localized periodic patterns for the non-symmetric generalized Swift-Hohenberg equation*, Phys. D, 208 (2005), pp. 73–95.

[18] B. Buffoni and J. F. Toland, *Global existence of homoclinic and periodic orbits for a class of autonomous Hamiltonian systems*, J. Diff. Eqns., 118 (1995), pp. 104–120.

[19] J. Burke and E. Knobloch, *Localized states in the generalized Swift-Hohenberg equation*, Phys. Rev. E, 73 (2006), p. 056211.

[20] ——, *Homoclinic snaking: structure and stability*, Chaos, 17 (2007), p. 037102.

[21] ——, *Normal form for spatial dynamics in the Swift-Hohenberg equation*, Discr. Cont. Dyn. Sys. Suppl., (2007), pp. 170–180. (September issue).

[22] ——, *Snakes and ladders: localized states in the Swift-Hohenberg equation*, Phys. Lett. A, 360 (2007), pp. 681–688.

[23] E. Buzano and M. Golubitsky, *Bifurcation on the hexagonal lattice and the planar Bénard problem*, Philos. Trans. Roy. Soc. London Ser. A, 308 (1983), pp. 617–667.

[24] B. J. Cantwell, *Introduction to Symmetry Analysis*, Cambridge University Press, Cambridge, 2002.

[25] S. J. Chapman and G. Kozyreff, *Exponential asymptotics of localised patterns and snaking bifurcation diagrams.* Preprint, 2008.

[26] P. Coullet, C. Riera, and C. Tresser, *Stable static localised structures in one dimension*, Phys. Rev. Lett., 84 (2000), pp. 3069–3072.

[27] S. M. Cox and P. C. Matthews, *Exponential time differencing for stiff systems*, J. Comput. Phys., 176 (2002), pp. 430–455.

[28] ——, *Instability and localisation of patterns due to a conserved quantity*, Phys. D, 175 (2003), pp. 196–219.

[29] C. Crawford and H. Riecke, *Oscillon-type structures and their interaction in a Swift-Hohenberg model*, Phys. D, 129 (1999), pp. 83–92.

[30] M. Cross and P. Hohenberg, *Pattern formation outside of equilibrium*, Rev. Mod. Phys., 65 (1993), pp. 851–1112.

[31] P. Davies, P. Blanchedeau, E. Dulos, and P. D. Kepper, *Dividing blobs, chemical flowers and patterned islands in a reaction-diffusion system*, J. Phys. Chem. A, 102 (1998), pp. 8236–8244.

[32] R. J. Deissler and H. R. Brand, *Two-dimensional localized solutions for subcritical bifurcations in systems with broken rotational symmetry*, Phys. Rev. E, 51 (1995), p. R852.

[33] B. Dionne, M. Silber, and A. C. Skeldon, *Stability results for steady, spatially periodic planforms*, Nonlinearity, 10 (1997), pp. 321–353.

[34] E. J. Doedel, auto07p*: continuation and bifurcation software for ordinary differential equations*, tech. rep., Concordia University, 2007.

[35] A. Doelman, B. Sandstede, A. Scheel, and G. Schneider, *Propagation of hexagonal patterns near onset*, European J. Appl. Math., 14 (2003), pp. 85–110.

[36] J. Eggers and H. Riecke, *Continuum description of vibrated sand*, Phys. Rev. E, 59 (1999), pp. 4476–4483.

[37] P. C. Fife, *Pattern formation in gradient systems*, in Handbook of Dynamical Systems 2, Elsevier, 2002, pp. 679–719.

[38] J. Fineberg, *Physics in a jumping sandbox*, Nature, 382 (1996), pp. 793–764.

[39] A. A. Golovin, B. J. Matkowsky, and A. A. Nepomnyashchy, *A complex Swift-Hohenberg equation coupled to the Goldstone mode in the nonlinear dynamics of flames*, Phys. D, 179 (2003), pp. 183–210.

[40] M. Golubitsky, I. Stewart, and D. G. Schaeffer, *Singularities and Groups in Bifurcation Theory II*, Springer-Verlag, New York, 1988.

[41] M. Golubitsky, J. W. Swift, and E. Knobloch, *Symmetries and pattern selection in Rayleigh-Bénard convection*, Phys. D, 10 (1984), pp. 249–276.

[42] D. Gomila, A. J. Scroggie, and W. J. Firth, *Bifurcation structure of dissipative solitons*, Phys. D, 227 (2007), pp. 70–77.

[43] M. A. Heroux, R. A. Bartlett, V. E. Howle, R. J. Hoekstra, J. J. Hu, T. G. Kolda, R. B. Lehoucq, K. R. Long, R. P. Pawlowski, E. T. Phipps, A. G. Salinger, H. K. Thornquist, R. S. Tuminaro, J. M. Willenbring, A. Williams, and K. S. Stanley, *An overview of the Trilinos project*, ACM Trans. Math. Softw., 31 (2005), pp. 397–423.

[44] M. F. Hilali, S. Metens, P. Borckmans, and G. Dewel, *Pattern selection in the generalised Swift-Hohenberg model*, Phys. Rev. E, 51 (1995), pp. 2046–2052.

[45] R. B. Hoyle, *Pattern Formation*, Cambridge University Press, Cambridge, 2006.

[46] G. W. Hunt, G. J. Lord, and A. R. Champneys, *Homoclinic and heteroclinic orbits underlying the post-buckling of axially-compressed cylindrical shells*, in Localization and solitary waves in solid mechanics, World Scientific Publishing, River Edge, 1999, pp. 285–297.

[47] G. W. Hunt, M. A. Peletier, A. R. Champneys, P. D. Woods, M. A. Wadee, C. J. Budd, and G. J. Lord, *Cellular buckling in long structures*, Nonlin. Dynam., 21 (2000), pp. 3–29.

[48] H. Jamgotchian, N. Bergeon, D. Benielle, P. Voge, B. Billia, and R. Guerin, *Localised microstructures induced by fluid flow in directional solidification*, Phys. Rev. Lett., 87 (2001), p. 166105.

[49] E. Knobloch, *Pattern selection in long-wavelength convection*, Phys. D, 41 (1990), pp. 450–479.

[50] ——, *Spatially localized structures in dissipative systems: open problems*, Nonlinearity, 21 (2008), pp. T45–T60.

[51] J. Knobloch and T. Wagenknecht, *Homoclinic snaking near a heteroclinic cycle in reversible systems*, Phys. D, 206 (2005), pp. 82–93.

[52] G. Kozyreff and S. J. Chapman, *Asymptotics of large bound states of localized structures*, Phys. Rev. Lett., 97 (2006), p. 044502.

[53] B. Krauskopf and T. Riess, *A Lin's method approach to finding and continuing heteroclinic connections involving periodic orbits*. Preprint, 2007.

[54] C. R. Laing and W. C. Troy, *PDE methods for nonlocal models*, SIAM J. Appl. Dyn. Syst., 2 (2003), pp. 487–516.

[55] C. R. Laing, W. C. Troy, B. Gutkin, and G. B. Ermentrout, *Multiple bumps in a neuronal model of working memory*, SIAM J. Appl. Math., 63 (2002), pp. 62–97.

[56] J. Lega, J. V. Moloney, and A. C. Newell, *Swift-Hohenberg equation for lasers*, Phys. Rev. Lett., 73 (1994), pp. 2978–2981.

[57] D. J. B. Lloyd and A. R. Champneys, *Efficient numerical continuation and stability analysis of spatiotemporal quadratic optical solitons*, SIAM J. Sci. Comput., 27 (2005), pp. 759–773.

[58] D. J. B. Lloyd and B. Sandstede, *Localized radial solutions in the Swift–Hohenberg equation*. In preparation, 2008.

[59] G. J. Lord, A. R. Champneys, and G. W. Hunt, *Computation of homoclinic orbits in partial differential equations: an application to cylindrical shell buckling*, SIAM J. Sci. Comput., 21 (1999), pp. 591–619.

[60] B. A. Malomed, A. A. Nepomnyashchy, and M. I. Tribelsky, *Domain boundaries in convection patterns*, Phys. Rev. A, 42 (1990), pp. 7244–7263.

[61] P. C. Matthews, *Hexagonal patterns in finite domains*, Phys. D, 116 (1998), pp. 81–94.

[62] P. C. Matthews, M. R. E. Proctor, and N. O. Weiss, *Compressible magnetoconvection in three dimensions: planforms and nonlinear behaviour*, J. Fluid Mech., 305 (1995), pp. 281–305.

[63] J. M. McSloy, W. J. Firth, G. K. Harkness, and G.-L. Oppo, *Computationally determined existence and stability of transverse structures II: multipeaked cavity solitons*, Phys. Rev. E, 66 (2002), p. 046606.

[64] M. Medelev, D. J. Srolovitz, L. Shvindlerman, and G. Gottstein, *Interface mobility under different driving forces*, J. Mater. Res., 17 (2002), pp. 234–245.

[65] I. Mercader, A. Alonso, and O. Batiste, *Spatiotemporal dynamics near the onset of convection for binary mixtures in cylindrical containers*, Phys. Rev. E, 77 (2008), p. 036313.

[66] A. Mielke, *A spatial center manifold approach to steady state bifurcations from spatially periodic patterns*, in Dynamics of nonlinear waves in dissipative systems: reduction, bifurcation and stability, G. Dangelmayr, B. Fiedler, K. Kirchgässner, and A. Mielke, eds., Longman, Harlow, 1996, pp. 209–262.

[67] ——, *Instability and stability of rolls in the Swift-Hohenberg equation*, Comm. Math. Phys., 189 (1997), pp. 829–853.

[68] A. A. Nepomnyaschy, M. I. Tribelsky, and M. G. Velarde, *Wave number selection in convection and related problems*, Phys. Rev. E, 50 (1994), pp. 1194–1197.

[69] L. A. Peletier and W. C. Troy, *Spatial Patterns*, Birkhäuser, Boston, 2001.

[70] M. A. Peletier, *Sequential buckling: a variational analysis*, SIAM J. Math. Anal., 32 (2001), pp. 1142–1168.

[71] D. Peterhof, B. Sandstede, and A. Scheel, *Exponential dichotomies for solitary-wave solutions of semilinear elliptic equations on infinite cylinders*, J. Diff. Eqns., 140 (1997), pp. 266–308.

[72] L. M. Pismen, *Patterns and Interfaces in Dissipative Dynamics*, Springer-Verlag, Berlin, 2006.

[73] Y. Pomeau, *Front motion, metastability, and subcritical bifurcations in hydrodynamics*, Phys. D, 23 (1986), pp. 3–11.

[74] M. I. Rabinovich, A. B. Ezersky, and P. D. Weidman, *The Dynamics of Patterns*, World Scientific Publishing, River Edge, 2000.

[75] P. H. Rabinowitz, *Periodic solutions of a Hamiltonian system on a prescribed energy surface*, J. Diff. Eqns., 33 (1979), pp. 336–352.

[76] ——, *The prescribed energy problem for periodic solutions of Hamiltonian systems*, in Hamiltonian Dynamical Systems, Amer. Math. Soc., Providence, 1988, pp. 183–191.

[77] S. Residori, *Patterns, fronts and structures in a liquid-crystal-light-valve with optical feedback*, Phys. Rep., 416 (2005), pp. 201–272.

[78] H. Sakaguchi and H. R. Brand, *Stable localised solutions of arbitrary length for the quintic Swift-Hohenberg equation*, Phys. D, 97 (1996), pp. 274–285.

[79] ——, *Stable localised squares in pattern-forming nonequilibrium systems*, Europhys. Lett., 38 (1997), pp. 341–346.

[80] ——, *Localised patterns for the quintic complex Swift-Hohenberg equation*, Phys. D, 117 (1998), pp. 95–105.

[81] B. Sandstede, *Stability of travelling waves*, in Handbook of Dynamical Systems II, B. Fiedler, ed., North-Holland, Amsterdam, 2002, pp. 983–1055.

[82] B. Sandstede and A. Scheel, *Defects in oscillatory media: toward a classification*, SIAM J. Appl. Dyn. Syst., 3 (2004), pp. 1–68.

[83] ——, *Relative Morse indices, Fredholm indices, and group velocities*, Discr. Cont. Dyn. Syst. A, 20 (2008), pp. 139–158.

[84] J. Shen, *Efficient spectral-Galerkin methods III: polar and cylindrical geometries*, SIAM J. Sci. Comput., 18 (1997), pp. 1583–1604.

[85] J. Swift and P. C. Hohenberg, *Hydrodynamic fluctuations at the convective instability*, Phys. Rev. A, 15 (1977), pp. 319–328.

[86] M. Tlidi, A. G. Vladimirov, and P. Mandel, *Interaction and stability of periodic and localised structures in optical bistable systems*, IEEE J. Quant. Electr., 39 (2003), pp. 216–226.

[87] L. N. Trefethen, *Spectral Methods in* matlab, SIAM, Philadelphia, 2000.

[88] L. S. Tsimring and I. S. Aranson, *Localised and cellular patterns in vibrated granular layer*, Phys. Rev. Lett., 79 (1997), pp. 213–216.

[89] P. B. Umbanhowar, F. Melo, and H. L. Swinney, *Localised excitations in a vertically vibrated granular layer*, Nature, 382 (1996), pp. 793–796.

[90] V. K. Vanag and I. R. Epstein, *Stationary and oscillatory localised patterns, and subcritical bifurcations*, Phys. Rev. Lett., 92 (2004), p. 128301.

[91] A. G. Vladimirov, J. M. McSloy, D. V. Skryabin, and W. J. Firth, *Two-dimensional clusters of solitary structures in driven optical cavities*, Phys. Rev. E, 65 (2002), p. 046606.

[92] P. D. Woods and A. R. Champneys, *Heteroclinic tangles and homoclinic snaking in the unfolding of a degenerate reversible Hamiltonian-Hopf bifurcation*, Phys. D, 129 (1999), pp. 147–170.